

FACULTY
OF MATHEMATICS
AND PHYSICS
Charles University

MASTER THESIS

Bc. Alexandr Dizov

Modeling orogeny on Venus

Department of Geophysics

Supervisor of the master thesis: Prof. RNDr. Ondřej Čadek, CSc.

Study programme: Geophysics and Planetary Science (N0533A110018)

Prague 2025

I declare that I carried out this master thesis on my own, and only with the cited sources, literature and other professional sources. I understand that my work relates to the rights and obligations under the Act No. 121/2000 Sb., the Copyright Act, as amended, in particular the fact that the Charles University has the right to conclude a license agreement on the use of this work as a school work pursuant to Section 60 subsection 1 of the Copyright Act.

In ..... date ....

Author's signature

First of all, I want to thank Prof. RNDr. Ondřej Čadek, CSc., my thesis supervisor, for his expert guidance, and for his patient support especially through the challenges of geoid modelling. Prof. Čadek gave me countless hours of enriching consultations (sometimes brightened by interesting cultural discussions). I would also like to thank RNDr. Petra Maireová, Ph.D., my technical consultant. I am truly grateful for her help during my first steps in ASPECT, all her advices during plugin development, and the testing approaches she suggested.

Special thanks to Mgr. Michaela Walterová, Ph.D., for spontaneously proofreading my thesis text and[1]. I'm also grateful to the Department of Geophysics for giving me the chance to present at EGU, it was both a fascinating and professionally rewarding experience. Of course, I have to thank Seven Illusions of Hanka Čížková for creating that (maybe overly) positive atmosphere in the PC lab. Thank you to our eleven cats, for keeping me sane, and to Marius Petipa (and other choreographers), whose art gave me many welcome escapes.

I would also like to acknowledge the ASPECT development team for creating and maintaining their geodynamic modelling software. I also wish to acknowledge the use of large language models (ChatGPT and DeepSeek). These LLMs were used exclusively for language refinement, grammatical correction, and text editing during the writing process.

Finally, my deepest thanks to my family for their constant understanding, patience, and never-ending support.

[1] introducing me to the art of footnotes

Title: Modeling orogeny on Venus

Author: Bc. Alexandr Dizov

department: Department of Geophysics

Supervisor: Prof. RNDr. Ondřej Čadek, CSc., Department of Geophysics

Abstract: The surface of Venus is covered with many various surface structures, the youngest and the most prominent of which is Atla Regio. So far, the uplift of this volcanic region was modelled only using unrealistic mantle plume while neglecting melting effects. We aimed to develop a model of Atla Regio uplift that includes both melting and a realistic plume consistent with upper mantle rheology. After a series of 2D and 3D simulations we were able to predict the short wavelength topography and geoid of Atla Regio. As a result we recieved the optimal parameters of the plume causing the uplift. However, our models revealed that Atla Regio is a much more complex region and our model requires further development in order to match the long wavelength observations.

Keywords: Venus, orogeny, numerical modeling, Atla Regio

Název práce: Modelování orogeneze na Venuši

Autor: Bc. Alexandr Dizov

Katedra: Katedra geofyziky

Vedoucí diplomové práce: Prof. RNDr. Ondřej Čadek, CSc., Katedra geofyziky

Abstrakt: Povrch Venuše je pokryt řadou různorodých útvarů, z nichž nejmladší a nejvýraznější je oblast Atla Regio. Doposud byl výzdvih této vulkanické oblasti modelován pouze pomocí nerealistického plášťového chocholu a bez zohlednění účinků tavení. Naším cílem bylo vytvořit model oblasti Atla Regio, který zahrnuje realistickou reologii a procesy tavení. Po sérii 2D a 3D simulací jsme dokázali předpovědět krátkovlnnou topografii a geoid Atla Regio a odhadnout parametry chocholu způsobujícího výzdvih této oblasti. Naše modely však odhalily, že Atla Regio má složitější strukturu, a pro soulad s dlouhovlnnými pozorováními je třeba náš model dále zdokonalit.

Klíčová slova: Venuše, orogenze, numerické modelování, Atla Regio

Contents

Introduction **9**

1 Methodology **11**
1.1 Model of the upper mantle 11
1.1.1 Temperature and governing equations 12
1.1.2 Generation of melt 12
1.1.3 Density and viscosity 13
1.1.4 Boundary conditions and the modelled domain 14
1.2 Calculation of the topography and the geoid 14
1.2.1 Model of the lower mantle 15
1.2.2 Topography 15
1.2.3 Geoid 18

2 Results **20**
2.1 2D models 20
2.1.1 Initial models and cohesion 20
2.1.2 Examined 2D models 21
2.1.3 Problems in 2D modelling 23
2.2 3D models 25
2.2.1 Qualitative examination of 3D models 25
2.2.2 Atla Regio models 26

3 Discussion **31**
3.1 Interpretation of the geoid 31
3.2 Further model development 33
3.3 Current limitations of the model 34
3.3.1 Melting model 34
3.3.2 Lateral lava mobility 35
3.3.3 Mantle rheology 37

Conclusion **39**

Bibliography **40**

List of Figures **43**

List of Tables **44**

List of Abbreviations **45**

A Topography, Gravity, and Geomorphology of Venus **47**
A.1 Available Data 47
A.2 Tectonic Regime of Venus 48
A.3 Atla Regio 48

B Tested 2D models **50**

C Chosen preliminary 3D models **54**

Introduction

In recent years, there has been an increasing interest in research of Venus among both geophysicists and planetary scientists. This increase is closely connected to three missions being in preparation to launch in the upcoming decade: VERITAS (Smrekar et al., 2022) and DAVINCI (Garvin et al., 2022) by NASA, and EnVision (Ghail et al., 2018) by ESA. These missions should significantly refine available data and could therefore improve our understading of evolution of Venus and its surface processes.

Venus datasets available today are, in comparison to Mars and Moon datasets, quite limited. These limitations arise predominantly from Venus's thick and dense atmosphere that poses a significant barrier to the research and mapping of Venus's surface. Main datasets available today are:

1. Magellan topography and gravity models produced by Konopliv et al. (1999) and Rappaport et al. (1999). The topography resolution is stated to be up to degree 360 and geoid up to degree 180 (although recent studies suggest that meaningful data are contained up to degree 60). Both topography and geoid are depicted in figure 1.

2. Synthetic Aperture Radar (SAR) imagery and global emissivity by Magellan (Johnson, 1991). This dataset offers global left-look and right-look imagery with resolution of 75 meters per pixel in microwave spectrum (12.6 cm).

3. Surface emissivity data provided by VIRTIS instrument of Venus Express (Svedhem et al., 2009). These measurements offer mapping of the southern hemisphere in infrared spectrum (1 μm) and have revealed potential recent volcanic activity.

A picture of a possible geologic history can be inferred from the available data. The history can be divided into 3 main eras: Fortunian, Guineverian and Atlian as explained in Ivanov et al. (2015). During the Fortunian era, most of the long wavelength topography highlands were formed. During Guineverian, vast lowland plains were formed due to the great resurfacing event. The Atlian era, the most recent and the most quiescent of them all, is the era of formation of lobate plains and big volcanic provinces. The most prominent feature of the Atlian era is Beta-Atla-Themis region (BAT) with characteristic extensive rifting system. Detailed global geomorphological analysis of different Cytherian terrains can be found in Ivanov and Head (2011).

Numerical research of global planetary convection reveals four main tectonic regimes: stangant lid, episodic lid, mobile lid and plutonic-squishy lid. In the context of Venus, usually only two of these regimes are considered possible. The episodic lid regime is characterised by long quiescent periods of lithospheric thickening and short episodic mantle overturns that lead to extensive volcanism (Armann and Tackley, 2012). It has been proposed that the Guineverian era could correspond to mantle overturn event and the current Atlian era is the quiet period between overturns. Another possibility for Venus is the plutonic-squishy lid (Lourenço et al., 2020) that is characterised by lithosphere being broken into many smaller crustal blocks (these could have been already identified in the plains

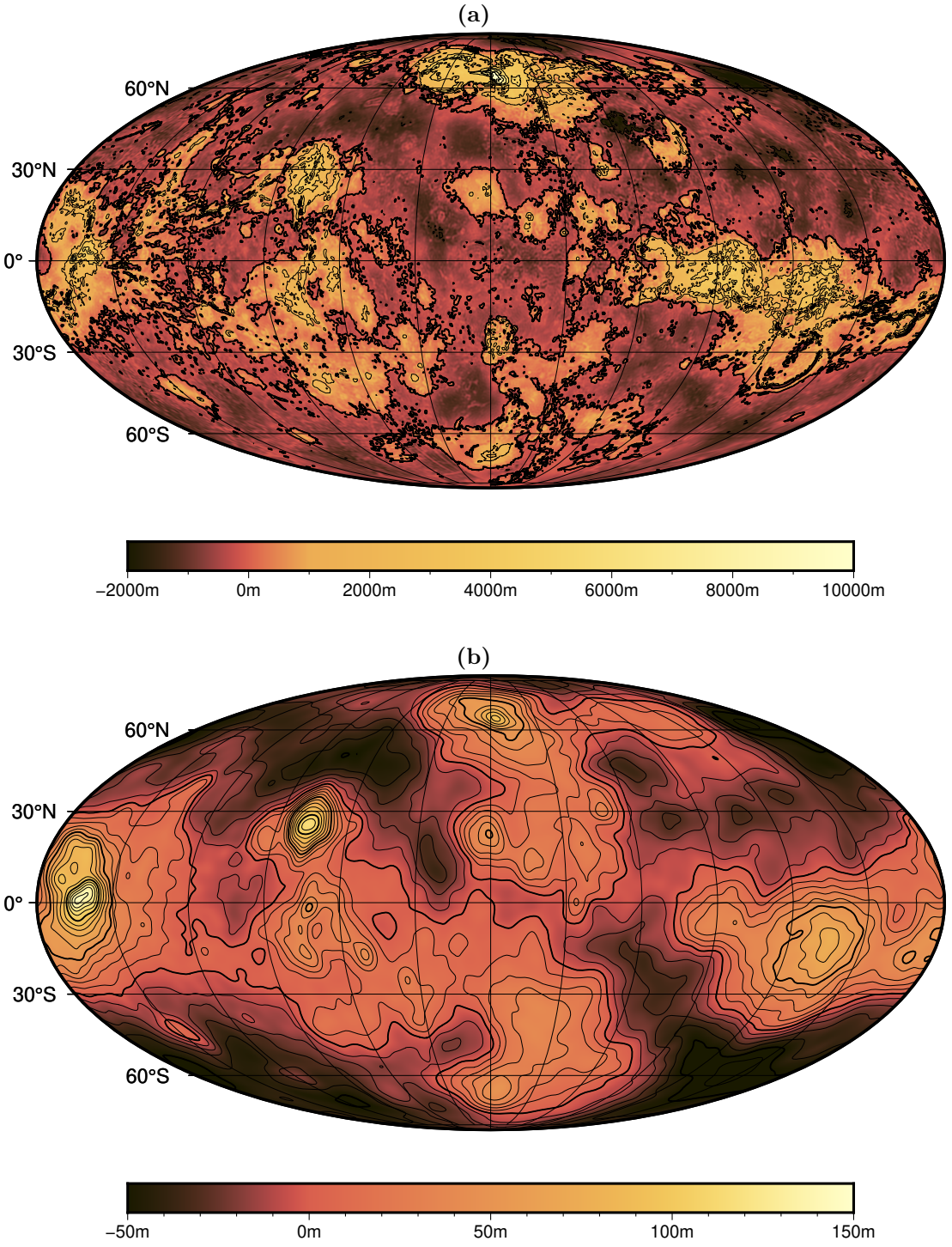


Figure 1 (a) Magellan topography up to degree 360, thin contours every 1500 m and thick contour at 0 m; (b) global geoid up to degree 60 with thin contours every 10 m and thick contours every 50 m.

regions by Byrne et al. (2021)) and the resurfacing occuring locally on a longer timescales.

One of the most prominent Cytherian features created during the Atlian era is Atla Regio (after which the era itself is named), located in the west part of the BAT region, in the heart of the rift network. Atla Regio is a large volcanic region consisting of multiple large volcanic edifices, namely Ozza Mons, Maat Mons and Ongwuti Mons. The topography of Atla Regio consists of two main peaks - one at Ozza Mons and another at Maat Mons. Analysis of the graben systems and lava outflow overlaps indicates that Ongwuti is the oldest of the volcanoes and Maat is the youngest (El Bilali et al., 2023). Also it is suggested that the uplift of Atla Regio began from the west (i.e. Ongwuti Mons) but later moved to the east (i.e. Ozza Mons). Available data for Atla Regio are shown in figure 2. See appendix A for a more detailed discription of current understanding of surface of Venus.

The question of formation of Regios has already been studied, both on a global scale (Maia et al., 2023; Pauer et al., 2006) and on a local scale (Vezolainen et al., 2004). Some works, where inversion of the geoid was performed, prescribed a radially homogeneous mantle plumes. In the case of Atla Regio, a columnar plume 700 km wide is prescribed, which is not realistic. The local scale model exploring the formation of Beta Regio is already working with a plume consistent with the chosen mantle viscosity structure, yet only the dynamic topography is considered and no melting effects are included. So far, we have failed to find any models of Atla Regio formation that would include a realistic plume and melting effects acting on the topography. In order to investigate the effects of melt on the Regio formation we introduce this, we believe pioneering, model of Regio formation that includes melting.

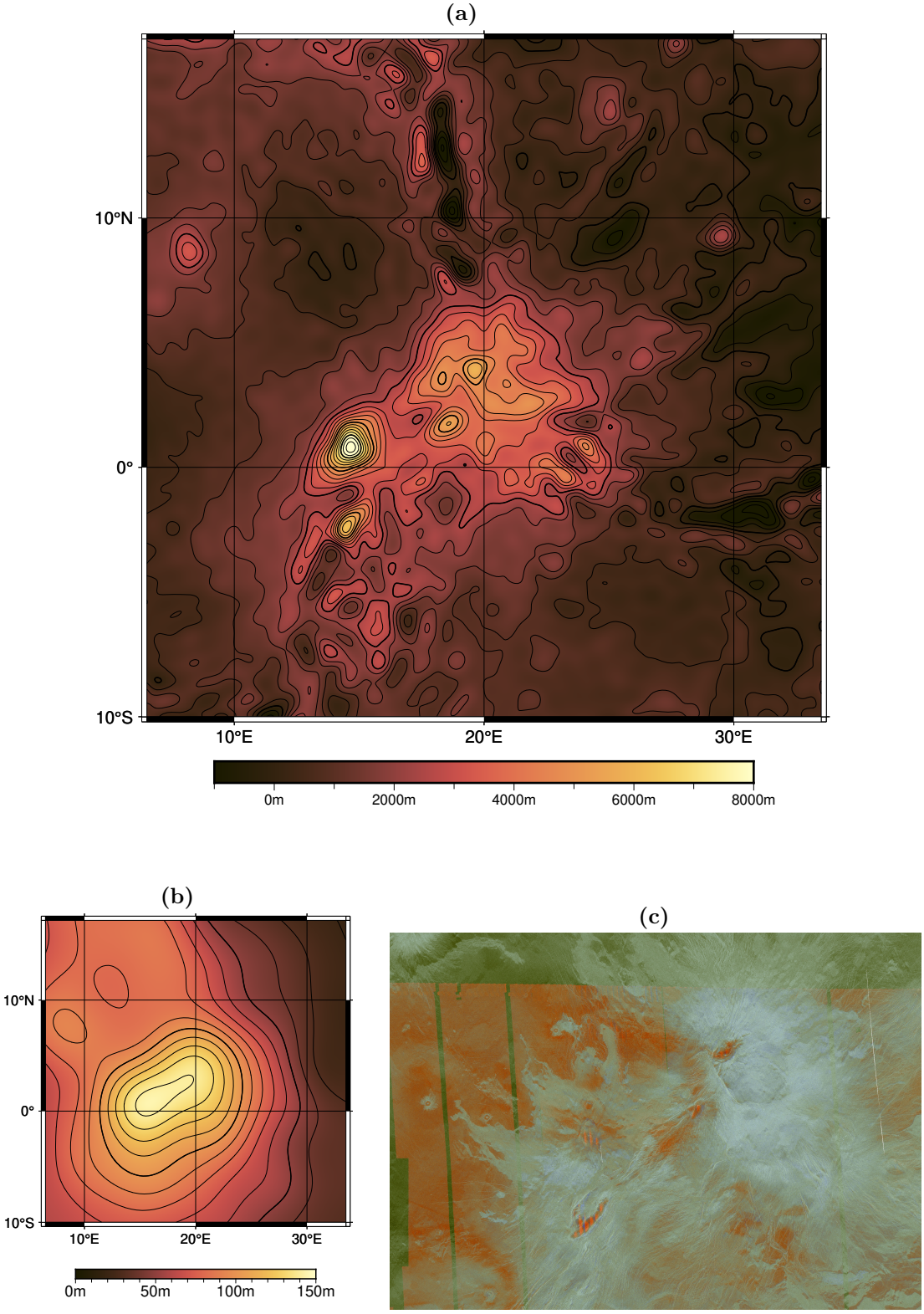


Figure 2 Data available for Atla Regio are (a) topography up to degree 360, thin contours every 500 m, thick contours every 2500 m; (b) geoid up to degree 60, thin contours every 10 m, thick contours every 50 m; (c) SAR map (both left-look and right-look) with color enhanced features.

1 Methodology

We investigate a possible scenario for Atla Regio uplift. We propose a single plume rising from the core mantle boundary (CMB), generating the dynamic topography at the surface. Once the plume reaches the top of the upper mantle, the plume head spreads at the base of the lithosphere. As the ascent of the plume is accompanied by decompression, the plume material melts and the magma is quickly extracted through the lid to the surface, where it solidifies and forms a layer of new basaltic rocks. These basaltic rocks deform the surface, contributing to both topography and geoid. The reaction of the surface is modelled by elastic flexure. In the later stages, the volcanic construct progressively reaches an isostatic equilibrium. For better understading of our model, reader is kindly asked to examine the figure 1.1. Furthermore, both hydrated and dehydrated mantle material hypotheses were examined.

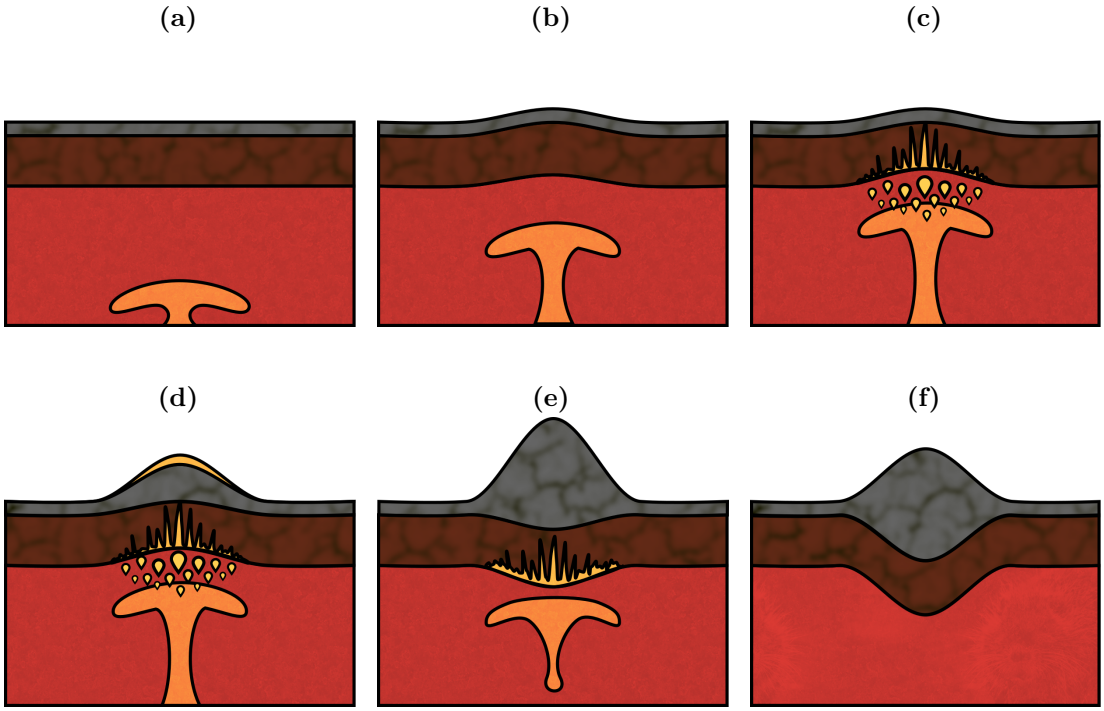


Figure 1.1 Proposed scenario of Atla regio evolution.(a) Initial stage with the source plume slowly rising from the lower mantle, (b) the plume reaches the upper mantle, dynamic topography is developed, (c) the plume reaches the base of the lithosphere, partial melting occurs and vertical magma channels (dikes) are formed in the lithosphere, (d) mantle keeps melting, magma is reaching the surface, creating a new crustal material and forming a volcanic construct, (e) transition to a plume-tail phase, melting rate decreases, the volcanic construct moves towards Airy isostasy, (f) late stage: the plume disappears, deposited crustal material is in Airy isostasy.

1.1 Model of the upper mantle

Our upper mantle model closely follows the approach outlined in Capitanio et al., 2024. Computations are done using the ASPECT code version 2.5.0, see

Heister et al., 2017; Kronbichler et al., 2012; Bangerth et al., 2023. To align with the ASPECT framework, the Capitanio model was adapted accordingly. Namely, we developed specialized material model plugin and a few postprocessor plugins that allow us to export needed variables (e.g. density variations and melt fraction on a grid) throughout the model domain.

The effects of lower mantle loading on the geoid values at the surface were calculated separately using spherical harmonics approach.

1.1.1 Temperature and governing equations

First, we define symbols for different temperatures using the following eq:

$$T = T_n + \frac{\alpha g T_{nr}}{c_p} d, \tag{1.1}$$

where T is the temperature, T_n is the non-adiabatic temperature, α is the thermal expansivity, g is gravity, T_{nr} is the radial non-adiabatic temperature profile, c_p is the thermal capacity and d is the depth. The second term on the right hand side represents the effects of the adiabatic compression. Since the lateral variations of T_n are small compared to T_{nr}, we can simplify equation (1.1) as follows:

$$T = T_n + \frac{\alpha g T_n}{c_p} d. \tag{1.2}$$

The non-adiabatic temperature is determined using the following equations:

$$\vec{\nabla} \cdot \vec{v} = 0, \tag{1.3}$$

$$-\vec{\nabla} \cdot \left[2\eta\left(T, F\right) \dot{\mathbf{e}}\right] + \vec{\nabla} p' = \Delta\rho\left(T_n, F\right) \vec{g}, \tag{1.4}$$

$$\rho_0 c_p \left(\frac{\partial T_n}{\partial t} + \vec{v} \cdot \vec{\nabla} T_n\right) - \vec{\nabla} \cdot \left(k \vec{\nabla} T_n\right) = \rho_0 h, \tag{1.5}$$

where $\vec{v}$ is the velocity vector, η is the viscosity, $\dot{\mathbf{e}}$ is the strain rate defined as $\dot{\mathbf{e}} = \frac{1}{2}\left(\vec{\nabla}\vec{v} + \left(\vec{\nabla}\vec{v}\right)^T\right)$, p' is the incremental pressure, $\Delta\rho$ is the density variation, $\vec{g}$ is the gravity vector, ρ_0 is the reference density, k is the thermal conductivity and h is the heat source density. Equation (1.3) is the continuity equation, (1.4) is the momentum equation and (1.5) is the heat transport equation. The symbol F represents mantle depletion, which is defined in the following section.

For simplicity, the gravity vector, heat sources, and all material parameters are considered constant, except for viscosity and density. The equations defining viscosity and density are presented in section 1.1.3.

1.1.2 Generation of melt

The model includes Rayleigh melting, also known as fractional melting, during which melt is extracted to the surface immediately. As melting occurs, the composition of the remaining mantle rocks changes, affecting both density and viscosity. These changes are primarily due to the extraction of volatiles, such as water, that migrate to the surface along with the melt. The weight fraction of melt extracted from the mantle rock is referred to as mantle depletion.

We define two new symbols: potential mantle depletion Φ and mantle depletion F. Potential mantle depletion represents the fraction of non-depleted mantle material that could melt completely under the current pressure and temperature conditions. In contrast, the mantle depletion describes the actual depletion of the mantle material resulting from melting. In reality, each time the mantle material produces some melt, it gets slightly more depleted. This process is irreversible, especially in our case when the melt is consistently extracted, thus the mantle depletion of the material point cannot decrease in time. Therefore, mantle depletion must reach the same value as the potential mantle depletion during melting, but it cannot decrease afterwards ($\frac{\mathrm{D}F}{\mathrm{D}t} \geq 0$, where $\frac{\mathrm{D}}{\mathrm{D}t}$ denotes the material time derivative).

The calculation of potential mantle depletion follows the theory of McKenzie and Bickle, 1988, incorporating the solidus and liquidus parameterizations from Katz et al., 2003 and is described by the following equations:

$$\Phi = \frac{1}{2} + T_{ss} + \left(T_{ss}^2 - \frac{1}{4}\right)(0.4259 + 2.988 T_{ss}), \tag{1.6}$$

$$T_{ss} = \begin{cases} \min\left(\frac{1}{2}; \max\left(\frac{T - \frac{T_{\mathrm{sol}}+T_{\mathrm{liq}}}{2}}{T_{\mathrm{liq}}-T_{\mathrm{sol}}}; -\frac{1}{2}\right)\right) & , d < 300\,\mathrm{km} \\ -\frac{1}{2} & , d \geq 300\,\mathrm{km} \end{cases}, \tag{1.7}$$

$$T_{\mathrm{sol}} = 1358.84\,\mathrm{K} + 132.9p\,\frac{\mathrm{K}}{\mathrm{GPa}} - 5.1p^2\,\frac{\mathrm{K}}{\mathrm{GPa}^2}, \tag{1.8}$$

$$T_{\mathrm{liq}} = 2053.14\,\mathrm{K} + 45.0p\,\frac{\mathrm{K}}{\mathrm{GPa}} - 2.0p^2\,\frac{\mathrm{K}}{\mathrm{GPa}^2}, \tag{1.9}$$

where T_{ss} is a non-dimensional parameter, T_{sol} is the solidus temperature, T_{liq} is the liquidus temperature and p is the total pressure in GPa. Solidus and liquidus models by Katz et al., 2003 are applicable only for pressures up to around 8 GPa, higher pressures lead to unrealistic solidus and liquidus temperatures. For this reason we allow melting only in the top 300 km of the model.

We calculate the mantle depletion assuming following equation:

$$F_{\vec{P}}(t) = \max_{t'<t}\left[\Phi\left(T_{\vec{P}}(t'), p_{\vec{P}}(t')\right)\right], \tag{1.10}$$

where $F_{\vec{P}}$ denotes the mantle depletion of the particle $\vec{P}$, and $T_{\vec{P}}$ and $p_{\vec{P}}$ represent temperature and pressure of the given particle $\vec{P}$.

1.1.3 Density and viscosity

Density in the model is considered linearly dependent on non-adiabatic temperature via thermal expansivity and linearly dependent on mantle depletion, as expressed in the following formula:

$$\Delta\rho = \rho_0\alpha\left(T_n - T_0\right) + \delta\rho_F F, \tag{1.11}$$

where α is the thermal expansivity, T_0 is the reference temperature and $\delta\rho_F = -72.6\,\mathrm{kg\,m^{-3}}$ is the density variation due to mantle's iron depletion. The density variations due to adiabatic effects $\rho_0\alpha\frac{\alpha\rho_0 T_n}{c_p}d$ can be omitted as those do not affect the solution of the velocity field calculated from equations (1.3) and (1.4).

The viscosity model uses both the temperature dependent diffusion creep as well as stiffening due to water depletion. Additionally, the Drucker-Prager yield criterium is implemented. For numerical reasons, minimum and maximum values of viscosity are introduced. Viscosity is calculated as:

$$\eta_{\mathrm{A,d}} = \eta_0 A^{\mathrm{diff}} \exp \frac{E_a^{\mathrm{diff}}}{R\left(T + \delta T_F F\right)} \left(1 - F\right)^{\frac{K-1}{K}}, \tag{1.12}$$

$$\eta_{\mathrm{D\text{-}P}} = \frac{C + \mu p}{2\dot{e}_{II}^D}, \tag{1.13}$$

$$\eta_u = \min\left(\eta_{\mathrm{A,d}}; \eta_{\mathrm{D\text{-}P}}\right), \tag{1.14}$$

$$\eta = \begin{cases} \eta_{\min} & , \eta_u < \eta_{\min} \\ \eta_u & , \eta_{\min} \leq \eta_u \leq \eta_{\max} \\ \eta_{\max} & , \eta_{\max} < \eta_u \end{cases} \tag{1.15}$$

where $\eta_{\mathrm{A,d}}$ is the Arrhenius viscosity with the effects of mantle depletion, η_0 is the reference viscosity, A^{diff} is the diffusion creep prefactor, E_a^{diff} is the diffusion activation energy, R is the molar gas constant, $\delta T_F = 260\,\mathrm{K}$ is the temperature change due to mantle depletion, simulating effects of the latent heat of melting, and K is the partition coefficient of water. The factor $\left(1 - F\right)^{\frac{K-1}{K}}$ stems from the assumption of Rayleigh melting. The values for all material parameters are given in chapter 2.

Symbol $\eta_{\mathrm{D\text{-}P}}$ denotes the Drucker-Prager effective viscosity, C is the cohesion, μ is the friction of the material, $\dot{e}_{II}^D$ is the square root of the second invariant of the deviator of the strain rate (second invariant is defined as $\frac{1}{2}\mathrm{tr}\,\dot{\mathbf{e}}^2$), η_u is the unbount viscosity, $\eta_{\min}$ is the minimum viscosity and $\eta_{\max}$ is the maximum viscosity.

1.1.4 Boundary conditions and the modelled domain

For simplicity, we model the upper mantle in Cartezian box (both 2D and 3D) with a depth of 730 km. This is the depth of ringwoodite to perovskite phase transition (on Earth it is located at a depth of 660 km). The gravity vector, $\vec{g} = 8.71\,\vec{e}_z\ \mathrm{m/\,s^2}$, is strictly vertical. Free slip is considered on all boundaries except for the bottom boundary where zero traction, i.e. open boundary, is implemented.

On the side boundaries, zero heat flux boundary condition is implemented. On the top boundary we prescribe $T_n = 723\,\mathrm{K}$ (average surface temperature of Venus), and on the bottom boundary $T_n = 1703\,\mathrm{K}$ (leading to $T = 1968\,\mathrm{K}$ which is the temperature of the phase transition). The heat source density is $6.5 \cdot 10^{-12}\,\mathrm{W/\,kg}$.

1.2 Calculation of the topography and the geoid

So far, we described the main part of our model which calculates the upper mantle convection caused by the upper mantle density variations. However, the convection caused by the lower mantle loading may play an important role in the total observed topography and geoid. In order to include the lower mantle in our model, a simple lower mantle parametric model is developed. This parametric model calculates the whole mantle convection caused by the lower mantle density

variations in the spherical geometry. The total topography and geoid is afterwards calculated in spectral domain by superponing solutions from the upper mantle model, which we first transform from cartezian to spherical geometry, and the parametric lower mantle model. See figure 1.2 for illustration.

1.2.1 Model of the lower mantle

We assume an isoviscous lower mantle and a single source plume coming from the CMB to the 730 km phase transition that causes the temperature and density variations in the lower mantle. The width of the plume is estimated from the continuity boundary condition at a depth of 730 km (where the upper mantle and lower mantle models have a mutual boundary). The velocities for the continuity boundary condition are estimated based on the empirical scaling law $v \sim \sqrt{\eta}$ (O. Čadek, personal communication, April 8, 2025). The approximate radius of the cyllindrical plume is calculated as:

$$r_{\mathrm{L}} = \sqrt{\frac{S_{\mathrm{U}}}{\pi}\sqrt{\frac{\eta_{\mathrm{low}}}{\eta_{\mathrm{upp}}}}}, \tag{1.16}$$

where r_{L} is the approximate radius of the plume in the lower mantle, S_{U} is the source area at the lower boundary of the upper mantle (i.e. the area where plume penetrates the 730 km phase transition), η_{upp} is the average viscosity in the upper mantle (excluding lithosphere) and η_{low} is the average viscosity in the lower mantle.

After calculating the approximate parameters of the plume in the lower mantle, we proceed to solve for the whole mantle convection (figure 1.2f) caused by the density variations in the lower mantle (figure (1.2d)). The velocity field is obtained by solving the following equations:

$$\vec{\nabla} \cdot \vec{v} = 0, \tag{1.17}$$

$$\vec{\nabla} \cdot \mathbf{t}^D = -\Delta\rho\vec{g}, \tag{1.18}$$

$$\mathbf{t}^D - 2\eta\dot{\mathbf{e}} = \mathbf{0}, \tag{1.19}$$

where $\mathbf{t}^D$ is the deviator of the Cauchy stress tensor and the rest of the variables were previously defined. Density anomaly $\Delta\rho$ is calculated based on the temperature contrast between the plume and the lower mantle temperature. We prescribed this temperature jump equal to the temperature anomaly of the plume on the lower boundary in our upper mantle model. Note that convection is calculated in the whole mantle, meaning also at the top boundary, but the source forces are located exclusively in the lower mantle (figure 1.2f).

The problem defined by equations (1.17), (1.18), and (1.19) is solved in spectral domain by standard decomposition into spherical harmonics with the dynamic topography boundary conditions. In the following subsections, lower indeces $\bullet_{,lm}$ indicate spherical harmonical coefficient (of the given variable) of degree l and order m.

1.2.2 Topography

In our model two sources of surface topography are considered. The first one is the dynamic topography that is calculated from the total vertical traction at

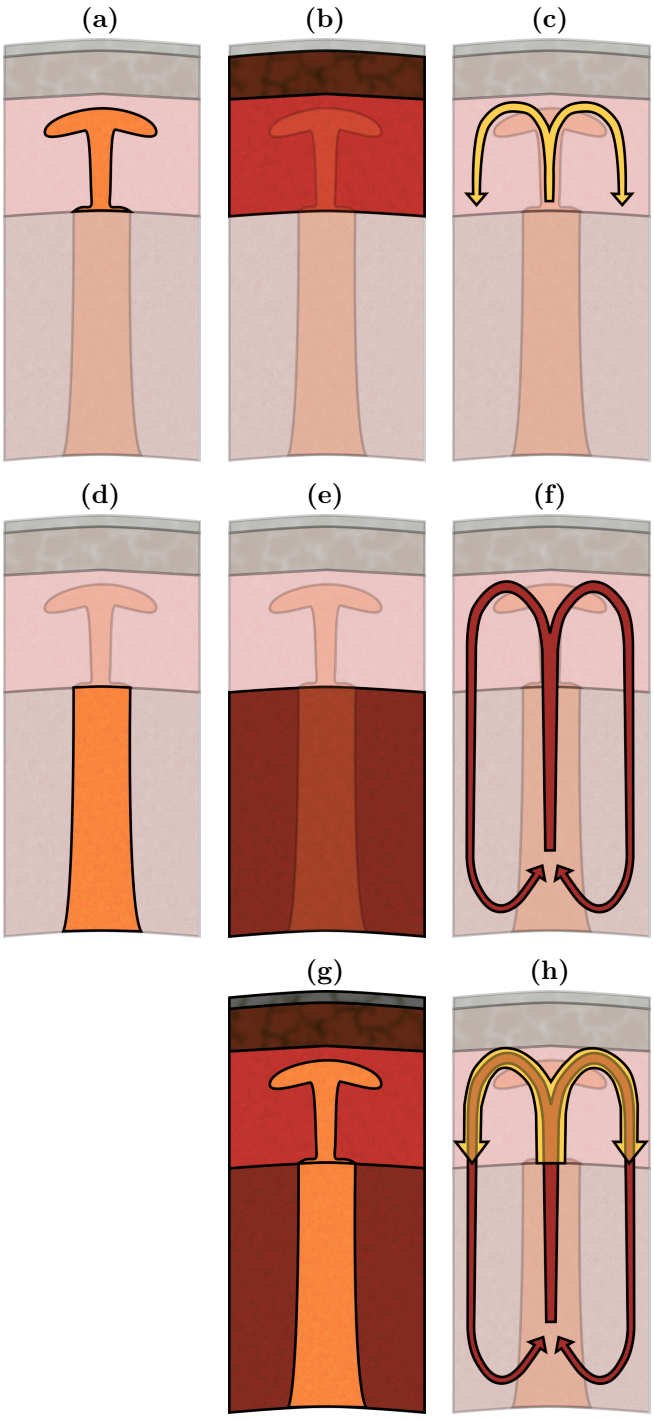


Figure 1.2 Illustration of the upper and lower mantle dynamics.

(a) The upper mantle density variations induced by the plume with bottom cross section S_{U}, located in (b) the upper mantle region with viscosity η_{upp}, causing (c) upper mantle convection (which is calculated in ASPECT).

(d) The lower mantle density variations induced by the plume with radius r_{L}, located in (e) the lower mantle region with viscosity η_{low}, causing (f) whole mantle convection (which is calculated in spectral domain).

(g) The full picture of the proposed mantle structure beneath Atla Regio, and (h) the total convection obtained by superponing the convection patterns (c) and (f).

the top boundary. The dynamic topography is determined from the following equation:

$$t_{\mathrm{D},lm} = \frac{\sigma_{\mathrm{UM},lm} + \sigma_{\mathrm{LM},lm}}{\rho_0 g}, \tag{1.20}$$

where t_{D} is the total dynamic topography at the surface, σ_{UM} and σ_{LM} are the surface vertical tractions caused by density variations in the upper mantle and in the lower mantle, respectively[1], ρ_0 is the reference density and g is the gravity acceleration. The lower mantle effects are omitted in 2D models.

The second source of the total topography is the crustal topography. This topography is the result of crustal growth caused by extrusive volcanism. The crustal topography is built in the following way:

1. In the upper mantle, the mantle depletion F is calculated. These values hold the information about the amount of melt that was generated from the given material point.

2. Increase in the mantle depletion at a given material point in time indicates new melt was generated.

3. Newly generated melt is thought to be quickly extracted to the surface via unspecified mechanism (could be the two phase flow, formation of dikes or some other).

4. The material newly emplaced on top of the crust increases the surface load. In 2D case we assume immediate isostatic compensation of the topography. However, in 3D models we include elastic behaviour of the lithosphere leading to an immediate elastic compensation.

The crustal topography including the elastic flexure is calculated using the analytical formula by Turcotte et al. (1981):

$$t_{\mathrm{C},lm} = \frac{\left(R - d_{\mathrm{ADC}}\right)^2 \left(\rho_0 - \rho_{\mathrm{C}}\right)}{C_l \rho_{\mathrm{C}} + \left(R - d_{\mathrm{ADC}}\right)^2 \left(\rho_0 - \rho_{\mathrm{C}}\right)} d_{\mathrm{C},lm}, \quad \text{in the spectral domain,} \tag{1.21}$$

$$d_{\mathrm{C}} = \int_{R_{730}}^{R} F \frac{\rho_{\mathrm{C}}}{\rho_0} \,\mathrm{d}z, \quad \text{in the space domain,} \tag{1.22}$$

where t_{C} is the crustal topography, R is the radius of Venus, d_{ADC} is the apparent depth of compensation (the mean depth where the crustal root supporting the topography should be located), ρ_0 is the reference density in the upper mantle, ρ_{C} is the density of the crustal material, C_l is the compensation coefficient taken from Turcotte et al. (1981), d_{C} is the crustal thickness, R_{730} is the radius where the 730 km phase transition is located and F is previously defined mantle depletion. The crustal thickness was calculated in ASPECT in the space domain and then transformed into spectral domain for further use.

The total topography is calculated as a sum of dynamic and crustal topographies (t_{D} and t_{C}, respectively):

$$t_{\mathrm{f},lm} = t_{\mathrm{D},lm} + t_{\mathrm{C},lm}, \tag{1.23}$$

[1]Once again we emphasize that σ_{UM} is computed from the convection, which is calculated in ASPECT in cartezian geometry and then transformed into spherical geometry, while σ_{LM} is computed directly in the spherical geometry.

where t_{f} is the total surface topography.

As of the CMB topography, we only include the stress caused by lower mantle loading:

$$t^{(b)}_{\mathrm{D}\ ,lm} = \frac{\sigma^{(b)}_{\mathrm{LM},lm}}{(\rho_{\mathrm{K}} - \rho_0)g}, \tag{1.24}$$

where $t^{(b)}_{\mathrm{D}}$ is the dynamic CMB topography, $\sigma^{(b)}_{\mathrm{LM}}$ is the vertical traction on the CMB caused by lower mantle loading, and $\rho_{\mathrm{K}} - \rho_0$ is the density jump at CMB.

1.2.3 Geoid

The geoid is calculated only for 3D models using classical spherical harmonics approach. Considered geoid contributions and density anomalies that cause them are given in the following table:

Geoid symbol Source radius Density variation	Description of the geoid contribution source Description of the source location Description of the density variation
$h^{(t)}_{\mathrm{C}}$ $r = R$ ρ_{C}	the surface crustal topography t_{C} Venus's surface crustal density
$h^{(t)}_{\mathrm{D}}$ $r = R$ ρ_0	the surface dynamic topography t_{D} Venus's surface mantle reference density
$h^{(r)}_{\mathrm{C}}$ $r = R - d_{\mathrm{ADC}}$ $\rho_0 - \rho_{\mathrm{C}}$	the crustal root topography $t_{\mathrm{C}} - d_{\mathrm{ADC}}$ depth of compensation, i.e. crust-mantle boundary mantle-crust density jump
h_{UM} $R_{730} < r < R$ $\Delta\rho$	the upper mantle density variations upper mantle density variations caused by thermal anomalies
h_{LM} $R_{\mathrm{CMB}} < r < R_{730}$ $\Delta\rho$	the lower mantle density variations lower mantle prescribed lower mantle density variations
$h^{(b)}_{\mathrm{D}}$ $r = R_{\mathrm{CMB}}$ $\rho_{\mathrm{K}} - \rho_0$	the CMB topography $t^{(b)}_{\mathrm{D}}$ CMB CMB density jump

Table 1.1 Considered density anomalies when calculating the geoid.

The geoid contributions are calculated in the spectral domain as follows:

$$h^{(t)}_{\mathrm{C}\ ,lm} = \frac{4\pi GR}{2l+1}\frac{\rho_{\mathrm{C}} t_{\mathrm{C},lm}}{g}, \tag{1.25}$$

$$h^{(t)}_{\mathrm{D}\ ,lm} = \frac{4\pi GR}{2l+1}\frac{\rho_{0} t_{\mathrm{D},lm}}{g}, \tag{1.26}$$

$$h^{(r)}_{\mathrm{C}\ ,lm} = \frac{4\pi GR}{2l+1}\left(\frac{R-d_{\mathrm{ADC}}}{R}\right)^{l+2}\frac{(\rho_0-\rho_{\mathrm{C}})\left(t_{\mathrm{C},lm}-d_{\mathrm{C},lm}\right)}{g}, \tag{1.27}$$

$$h_{\mathrm{UM},lm} = \frac{4\pi GR}{2l+1}\int\limits_{R_{730}}^{R}\left(\frac{r'}{R}\right)^{l+2}\frac{\Delta\rho(r')_{,lm}}{g}\,\mathrm{d}r', \tag{1.28}$$

$$h_{\mathrm{LM},lm} = \frac{4\pi GR}{2l+1}\int\limits_{R_{\mathrm{CMB}}}^{R_{730}}\left(\frac{r'}{R}\right)^{l+2}\frac{\Delta\rho(r')_{,lm}}{g}\,\mathrm{d}r', \tag{1.29}$$

$$h^{(b)}_{\mathrm{D}\ ,lm} = \frac{4\pi GR}{2l+1}\left(\frac{R_{\mathrm{CMB}}}{R}\right)^{l+2}\frac{(\rho_{\mathrm{K}}-\rho_0)\,t^{(b)}_{\mathrm{D}\ ,lm}}{g}, \tag{1.30}$$

$$h_{\mathrm{t},lm} = h^{(t)}_{\mathrm{C}\ ,lm} + h^{(t)}_{\mathrm{D}\ ,lm} + h^{(r)}_{\mathrm{C}\ ,lm} + h_{\mathrm{UM},lm} + h_{\mathrm{LM},lm} + h^{(b)}_{\mathrm{D}\ ,lm}, \tag{1.31}$$

where h_{t} represents the total surface geoid.

2 Results

2.1 2D models

As previously mentioned, the model domain is a rectangle with a depth of 730 km and a width of 7300 km. Such a wide model domain is chosen to minimize the effect of the side boundaries. Material parameters of our models are listed in table 2.1, the values are taken from Capitanio et al. (2024).

Parameter	Value
ρ_0 - reference density	$3300\,\mathrm{kg/\,m^3}$
c_p - thermal capacity	$1200\,\mathrm{J\,K^{-1}\,kg^{-1}}$
k - thermal conductivity	$3.96\,\mathrm{W\,m^{-1}\,K^{-1}}$
α - thermal expansivity	$3 \cdot 10^{-5}\,\mathrm{K^{-1}}$
η_0 - reference viscosity	$10^{20}\,\mathrm{Pa\,s}$
A^{diff} - diffusion creep prefactor	$[10^{-9}; 10^{-6}]$
E_a^{diff} - activation energy	$2.4 \cdot 10^5\,\mathrm{J/\,mol}$
μ - Drucker-Prager friction coefficient	0.013[a]
C - Drucker-Prager cohesion	$[0.5; 50]\,\mathrm{MPa}$
η_{min} - minimum viscosity	$[10^{19}; 1.2 \cdot 10^{20}]\,\mathrm{Pa\,s}$
η_{max} - maximum viscosity	$10^{24}\,\mathrm{Pa\,s}$
K - water partition coefficient	$2.1 \cdot 10^{-2}$

Table 2.1 Material parameters

[a]The value is taken from Capitanio et al. (2024)

As a result of our approach, the viscosity structure of the upper mantle consists of three layers. In the lithosphere, viscosity is primarily controlled by the maximum viscosity (η_{max}). In the sublithospheric mantle, viscosity is controlled by the minimum viscosity (η_{min}). And in the area in between, viscosity is controlled by the diffusion creep parameters (η_0, A^{diff} and E_a^{diff}). Note that, as a consequence, increasing the minimum viscosity η_{min} directly increases the viscosity in the sublithospheric mantle.

In order to obtain a well-mixed and thermally evolved system, first 1.5 Gy of evolution are modelled without melting effects. The obtained temperature distribution is used as the initial condition for the rest of the models that include both melting and a plume entering the domain from the lower mantle.

The tectonic regime is mainly determined by Drucker-Prager cohesion. As in this work we assume an episodic lid regime, we first need to determine the cohesion that leads to this specific regime.

2.1.1 Initial models and cohesion

If we exclude intrusive magmatism, then the only parameter determining the tectonic regime is cohesion: low cohesions lead to the mobile lid regime, medium cohesions lead to the episodic lid regime, and high cohesions lead to the stagnant lid regime. Individual regimes can be distinguished by analysing the time

evolution of root mean square (RMS) velocity and the total heat flux through the top boundary, see figure 2.1.

The cohesion values that lead to an episodic lid regime are 10 MPa and 20 MPa. However, if the lithosphere is weak, a rising plume can trigger an overturn event. Since such a behaviour is not the focus of this work, we choose a cohesion 50 MPa. Even though such a high cohesion leads to a stagnant lid regime, the results remain valid for an episodic lid regime because, during the periods of tranquility, an episodic lid regime behaves identically to a stagnant lid regime. Furthermore, studies of Venus's rift systems (Foster and Nimmo, 1996) show that Venus's cohesion is around 80 MPa, much higher than on Earth. As a result, Earth-like values (10 MPa to 20 MPa) are not suitable for modelling Cytherian tectonics.

2.1.2 Examined 2D models

Due to the large number of tested models, we only provide a qualitative overview of main model parameters and their effects on melting processes.

First, we set the mantle viscosity $\eta_{\min} = 10^{20}$ Pa s and the diffusion creep prefactor $A^{\text{diff}} = 9.2 \cdot 10^{-9}$. With these values fixed, we vary the individual plume parameters. The effect of these parameters on melting is described below.

1. **Temperature of the plume** has a significant effect on the amount of melt produced above the plume. Our results reveal that the minimum temperature contrast, required for melting to occur, is between 50 K and 75 K. If the temperature is higher, more melt is produced. If the temperature is lower, plume's buoyancy is insufficient to thin the lithosphere and the hot material does not reach low pressures necessary for decompression melting. We tested the temperature contrast in the range from 25 K to 150 K.

2. **Radius of the plume** affects the melt production similarly to plume temperature. For fixed temperature contrast 75 K, melting occurs only at radii greater than 70 km. If the plume radius is smaller, then the buoyancy is not strong enough to thin the lithosphere. If the plume radius is bigger, we observe the same behaviour as if the temperature was increased, i.e. more melting and higher surface topography. We tested the plume radius in the range from 25 km to 80 km.

3. **Plume activity time**, defined as the duration during which the plume (i.e. the non-uniform lower boundary condition) is active, affects the length of the melting phase. The minimum activity time is around 100 My. If the activity time is shorter, the plume does not have enough time to thin the lithosphere sufficiently, and therefore no melting occurs[1]. We tested the activity time in the range from 50 My to 175 My.

In conclusion, we observe that once melting occurs, both temperature and radius of the plume play a similar role in the resulting melting processes.

[1] If the activity time is longer, then each plume that produces melt eventually reaches a point in time, when the mantle is already depleted and no more melt is produced. Since Atla Regio is most certainly still in plume-head phase (El Bilali et al., 2023), we do not discuss this effect further as it appears in a later stage. Nevertheless, this effect could be important for other Regios, such as Beta Regio, which is believed to be older (Vezolainen et al., 2004).

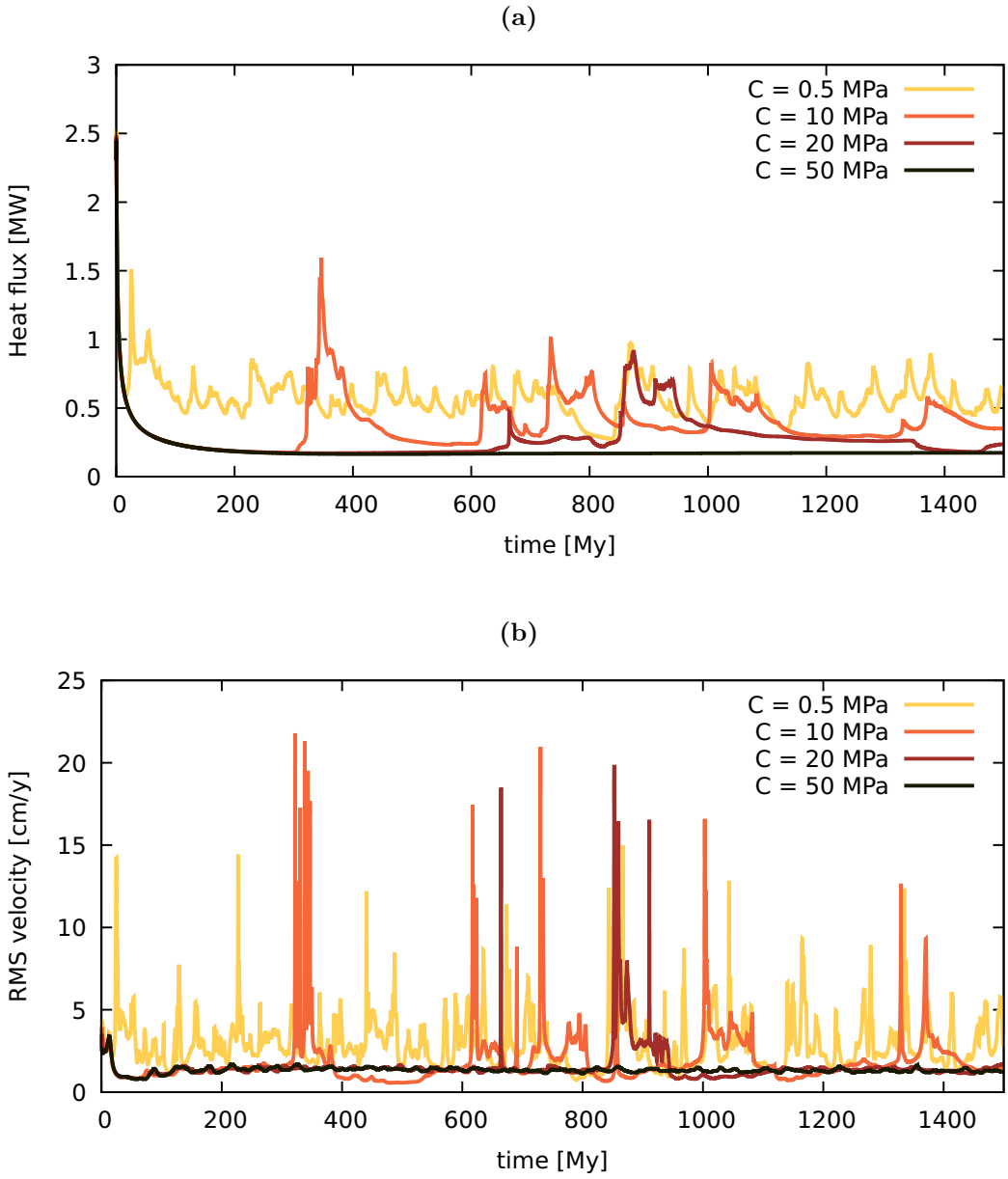


Figure 2.1 (a) Total heat flux through the top boundary and (b) RMS velocity in the upper mantle. A mobile lid regime ($C = 0.5$ MPa) is characterised by consistently high surface heat flux and high RMS velocity. An episodic lid regime ($C = 10$ MPa and $C = 20$ MPa) shows characteristic periods of overturn events (peaks in heat flux and RMS velocity) and tranquil periods in between (lower heat flux and RMS velocity). A stagnant lid regime ($C = 50$ MPa) has no peaks in heat flux or RMS velocity. Note that, during the periods of tranquility, an episodic lid regime with higher cohesion behaves identically to a stagnant lid regime.[a]

[a] In the case of the model with $C = 20$ MPa, the heat flux does not return to typical stagnant lid values following the overturn event around 900 My. Instead, it remains unexpectedly high. Closer analysis revealed a moving mid ocean ridge-like feature that persisted until it reached the right boundary around 1350 My, at which point it vanished and the heat flux dropped to stagnant lid levels.

Now, we examine the effect of other rheological parameters. We prescribe a plume with a radius of 70 km, temperature contrast of 75 K and activity time of 100 My. With these plume parameters fixed, we vary the following rheological parameters and study their effects on the melt production.

1. **Diffusion creep prefactor** primarily controls the thickness of the lithosphere[2]. The maximum prefactor, that still leads to melt occuring, is found to be around $1.8 \cdot 10^{-8} = 10^{-7.75}$. When the prefactor is greater, the lithosphere is thick and the plume cannot thin it. A smaller prefactor leads to initally thinner lithosphere, which is easier to thin further. In some cases, the lithosphere is so thin that decompression melting of the plume material begins already below the lithosphere and therefore no thinning is required.

2. **Minimum viscosity** controls the viscosity of the sublithospheric mantle. If the minimum viscosity is decreased, then it becomes easier for the plume to spread below the lithosphere. This results in the plume not thinning the lithosphere sufficiently and therefore less melt is produced. In the case of our fixed plume, melting occurs only for minimum viscosity higher than $0.8 \cdot 10^{20}$ Pa s.

3. **Cohesion** is the parameter that determines the stiffness of the lithosphere. If we further increase cohesion, then the plume's ability to thin the lithosphere decreases, which results in decreased melt production.

4. Both **melting postprocessor resolution** and **finite elements resolution** were also altered, but fortunately results showed almost no differences.

A more detailed overview of tested 2D models is presented in appendix B.

2.1.3 Problems in 2D modelling

One of the main problems we experience when running simulations in 2D is a phenomenon of a very high and narrow topographic peak. We illustrate the appearance of this peak in figure 2.2. The three stages shown in the figure are characteristic of all 2D models that produce sufficient amount of melt.

No tested model simultaneously produces topography high enough to match the data, and avoids the narrow peak anomaly. In models with high cohesion this narrow peak anomaly is not so strong, but these models either do not produce enough melt, or their melting area is too wide. We can speculate that a crustal material with high cohesion could help avoid the narrow peak anomaly, but we do not test this hypothesis further.

The main cause of melt appearing in a triangular area (that leads to the narrow peak) is modelling in 2D. In our 2D model, the plume resembles a wall-like structure in 3D, whereas real plumes are cylindrical. A wall-like plume could cause rifting in a realistic setting, but a cylindrical plume is generally not strong enough to tear the lithosphere apart[3] and therefore no rift-like melting will occur.

[2]However, if the prefactor is greater than 10^{-7}, the diffusion creep viscosity becomes greater than the minimum viscosity throughout the upper mantle. Because of this, the sublithospheric mantle viscosity is no longer controlled by the minimum viscosity $\eta_{\min}$.

[3]That is because a wall-like plume needs to tear the lithosphere only in one direction, whereas a cylindrical plume has to tear it in all directions.

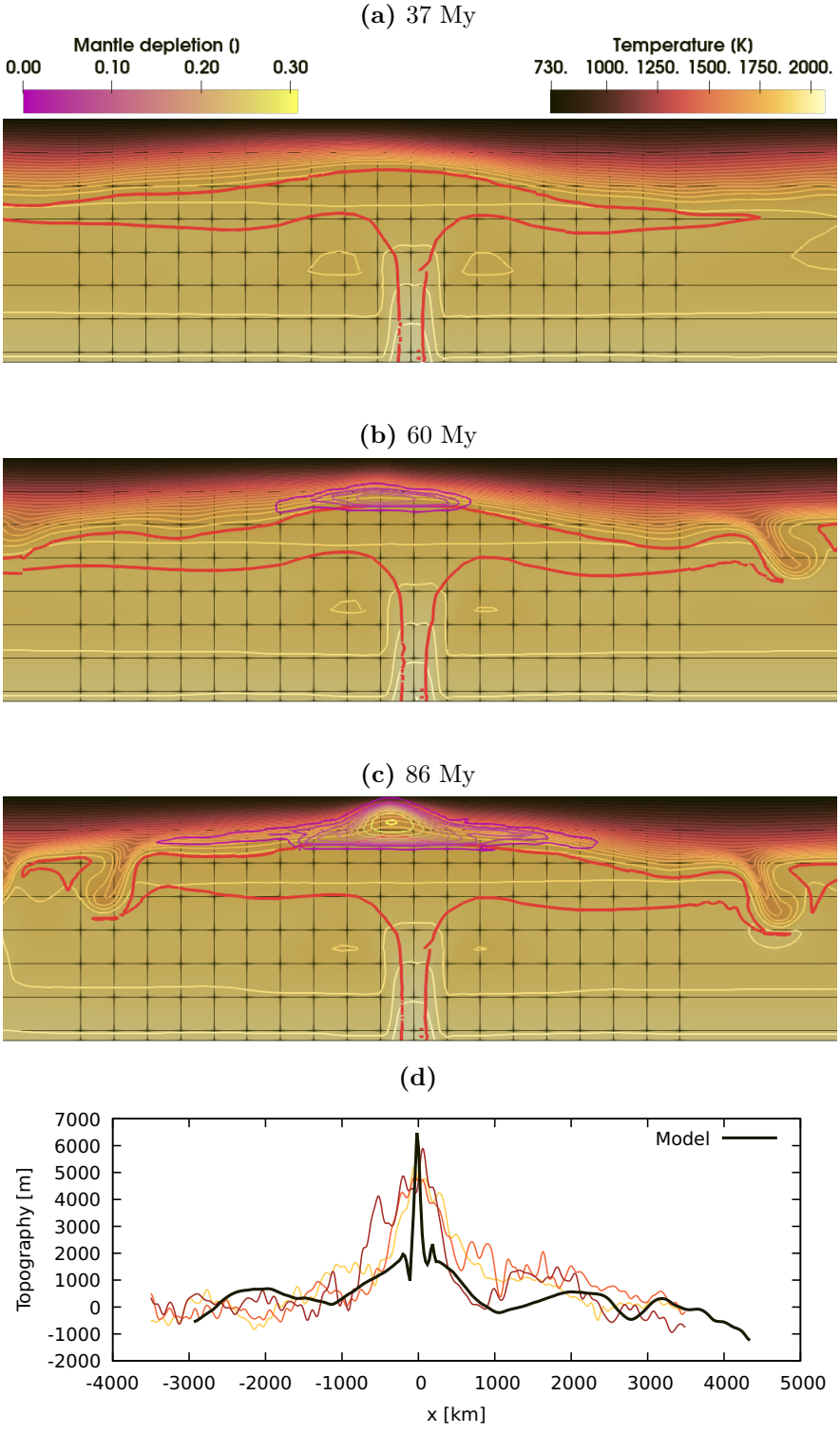


Figure 2.2 (a) The lithosphere is thinning above the rising plume (red contour). (b) Once the lithosphere is sufficiently thin, decompression melting occurs in a lens-shaped area. (c) In the later stage, the lithosphere is torn apart and additional melting occurs in a triangle-shaped area. This additional melting leads to (d) a very high and narrow topographic peak (black line) that is not observed in data (coloured lines). Figures (a-c) are cut off on the sides, their grid[a] spacing is 100 km.

[a]Coordinates grid drawn in figures (a-c) to show the figures' spatial scale.

2.2 3D models

The model domain is a 3D box with a vertical extent of 730 km and horizontal extents of 2920 km × 2920 km. We do not use a wider domain because if we widened the domain, the computational time would increase drastically. The initial conditions for all our 3D models are obtained by evolving a convection model for 1.5 Gy without melting.

2.2.1 Qualitative examination of 3D models

Based on Capitanio et al. (2024) and the results of 2D modelling, we set the material parameters $\eta_{\min} = 10^{20}$ Pa, $A^{\text{diff}} = 9.2 \cdot 10^{-9}$ and $C = 50$ MPa, the rest of parameters is listed in figure 2.1. Dynamic effects of mantle depletion are neglected. Our first model, where we prescribe a plume with the temperature contrast 75 K and the radius 70 km, shows that such plume is not able to produce any melt whatsoever. For that reason, we raise the plume temperature contrast to 100 K, at which point melting starts to occur. Next we run preliminary models A, B and C (see figures C.1, C.2 and C.3 respectively) to test the effect of the plume temperature and the minimum viscosity on the melt production in the system.

A Increased **minimum viscosity** (10^{21} Pa s instead of 10^{20} Pa s) leads to no melting. This is caused by smaller influx of hot material from the lower mantle[4] as well as more efficient cooling of this ascending material[5].

B Increase in **plume temperature contrast** (from 100 K to 150 K) significantly increases both plume buoyancy and melt production, which leads to high crustal and dynamic topographies. Relatively low sublithospheric viscosity causes intensive spreading of the hot plume under the lithosphere. The resulting topography matches Ozza Mons in height but is significantly wider. The amount of produced melt is approximately $38 \cdot 10^6$ km^3 (in the latest stage of model evolution). In comparison, Earth's large igneous provinces (LIPs) produce around $7 \cdot 10^6$ km^3 of melt (C. G. Farnetani, personal communication, April 29, 2025).

C If both **minimum viscosity** and **plume temperature contrast** are increased (minimum viscosity $\eta_{\min} = 10^{21}$ Pa s and temperature contrast 150 K), the plume becomes buoyant enough to lift the lithosphere and cause melting, and higher viscosity decreases plume's ability to spread beneath the lithosphere. As a result, we get enough melt to create topographic rise with height and extent comparable to Ozza Mons. The total volume of generated melt is approximately $6 \cdot 10^6$ km^3.

Testing the finite element resolution reveals that areas with small amount of melt tend to strongly overestimate the melt production. This only significantly affects model B, as model C does not exhibit any major resolution-dependent artifacts.

[4]Higher viscosity reduces convective velocities, decreasing influx.

[5]Higher viscosity leads to smaller convective velocities which allows more time for cooling via conduction.

2.2.2 Atla Regio models

We further optimize model C from the previous section to fit the observed Ozza Mons topography and geoid. The best-fit model is found using a local minimization method.

Misfit definition

The misfit is computed as the surface sum consisting of residuals from both topography and geoid. To reduce the influence of surface features that are not related to Ozza Mons, we apply several filters:

1. **Ozza Mons filter**, denoted as f_{Ozza}, is applied to limit the influence of residuals from the points that are outside of Ozza Mons (for example rifting zones to the North, South-West and East). This filter is a window-pass filter and is defined as:

$$f_{\mathrm{Ozza}}(x,y) = \exp\left(-\frac{(x-x_{\mathrm{Ozza}})^2 + (y-y_{\mathrm{Ozza}})^2}{2\sigma_{\mathrm{Ozza}}^2}\right), \tag{2.1}$$

   where x_{Ozza} and y_{Ozza} are x and y coordinates of Ozza Mons summit and σ_{Ozza} controls the radius of the filtering window. We set $\sigma_{\mathrm{Ozza}} = 365\,\mathrm{km}$ as that is the highest value that still suppresses the signal of topographic lows to the East and rises to the North-West.

2. **Maat Mons filter**, denoted as f_{Maat}, is applied because of the strong signal of Maat Mons volcano (located to the South-West from the Ozza Mons summit, near the equator).The Ozza Mons filter does not effectively remove the influence of Maat Mons because it is too close to Ozza Mons, and exhibits extremely high topography (over 8 km) and geoid (almost 150 m). Maat Mons filter is defined as:

$$f_{\mathrm{Maat}}(x,y) = 1 - \exp\left(-\frac{(x-x_{\mathrm{Maat}})^2}{2\left(\sigma_{\mathrm{Maat}}^{(x)}\right)^2} - \frac{(y-y_{\mathrm{Maat}})^2}{2\left(\sigma_{\mathrm{Maat}}^{(y)}\right)^2}\right), \tag{2.2}$$

   where x_{Maat} and y_{Maat} are x and y coordinates of the summit of Maat Mons and $\sigma_{\mathrm{Maat}}^{(x)}$ and ${\sigma^{(y)}}_{\mathrm{Maat}}$ are extents of the filtering window in respective directions. We set $\sigma_{\mathrm{Maat}}^{(x)} = 292\,\mathrm{km}$ and $\sigma_{\mathrm{Maat}}^{(y)} = 219\,\mathrm{km}$ as these are the smallest values that still filter out the Maat Mons data signal.

3. **Spectral filtering**, denoted as a functional $\hat{f}_{\mathrm{SH}}(\bullet)$, is applied due to significant long-wavelength geoid signal in Atla Regio. When applying this filter, we exclude those spherical harmonical coefficients that are of degrees higher than 60 (as these do not contain meaningful geoid data) and lower than 18 (as these contain features larger than Ozza Mons).

Moreover, we need to apply additional weighting to balance the residuals from the topography and the geoid. We rescale the geoid by a factor of $F_{tg} = 55$ based on the maxima of spectrally filtered topography and gravity data ($\hat{f}_{\mathrm{SH}}(t_{\mathrm{obs}})$ and $\hat{f}_{\mathrm{SH}}(h_{\mathrm{obs}})$, respectively). Finally, we then define misfit as a function:

$$L = \sum_{x,y} f_{\mathrm{Ozza}} f_{\mathrm{Maat}} \left[\left(\hat{f}_{\mathrm{SH}}(t_{\mathrm{f}}) - \hat{f}_{\mathrm{SH}}(t_{\mathrm{obs}})\right)^2 + F_{tg}^2\left(\hat{f}_{\mathrm{SH}}(h_{\mathrm{t}}) - \hat{f}_{\mathrm{SH}}(h_{\mathrm{obs}})\right)^2\right], \tag{2.3}$$

where L is the misfit, t_f is the total topography obtained from the evaluated model, t_obs is the observed topography, h_t is the total geoid generated by the evaluated model and h_obs is the observed geoid.

The summation is done over grid points (x, y) of the modelled surface and f_Maat, f_Ozza, $\hat{f}_\mathrm{SH}(t_\mathrm{f})$, $\hat{f}_\mathrm{SH}(t_\mathrm{obs})$, $\hat{f}_\mathrm{SH}(h_\mathrm{t})$ and $\hat{f}_\mathrm{SH}(h_\mathrm{obs})$ are, of course, evaluated at each surface point (x, y).

Misfit minimization

The gradient descent method is used to find the best-fit model. The varied model parameters are plume temperature contrast, plume radius, elastic thickness of the lithosphere, and crustal thickness (depth of compensation). To estimate the gradient, we compute the misfit of nearby models (each differing in only one parameter from the evaluated model) and then calculate the approximated gradient using finite differences. An overview of individual minimization steps is given in table 2.2.

Model name	temperature [K]	radius [km]	
	elastic th. [km]	crustal th. [km]	misfit [m^2]
20-ATLA-A [a]	150	90	
	30	35	$3.6377 \cdot 10^8$
B1	156	98	
	29.998	35.009	$3.6813 \cdot 10^8$
B2	162	106	
	29.996	35.018	$3.941 \cdot 10^8$
B3	168	114	
	29.994	35.027	$3.865 \cdot 10^8$
C1	154.1	98.6	
	29.980	35.014	$3.6506 \cdot 10^8$
C2	152.2	99.2	
	29.962	35.019	$3.6180 \cdot 10^8$

Table 2.2 Individual tested models during the minimization.

[a] We do not consider this initial model as the best-fit model, because its misfit minimum is observed at a geologically unrealistic time.

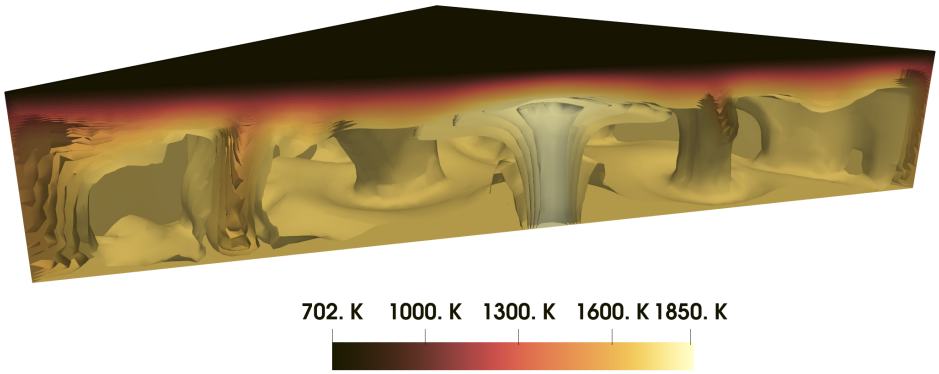
As we see, our initial guess (model 20-ATLA-A which is based on the model C, see figure C.3) is already very close to the optimal model C2. However, gradient descent further refined the plume radius and temperature to improve the model fit. Notably, the misfit appears to be insensitive to changes in elastic and crustal thicknesses, although elastic flexure is used when calculating the topography. Further testing revealed that elastic thickness affects the misfit significantly only at higher values around 100 km.

Model evolution and the optimal model C2

All tested 3D models that produce topography and geoid comparable to Ozza Mons, share a similar evolutionary pattern that is summarized in figures 2.3 and 2.4. The upper mantle temperature and mantle depletion of our best-fit model C2 are

depicted in figure 2.5. In figure 2.6 we compare the predicted topography and geoid to the measured data.

(a) Non-adiabatic temperature



(b) Mantle depletion

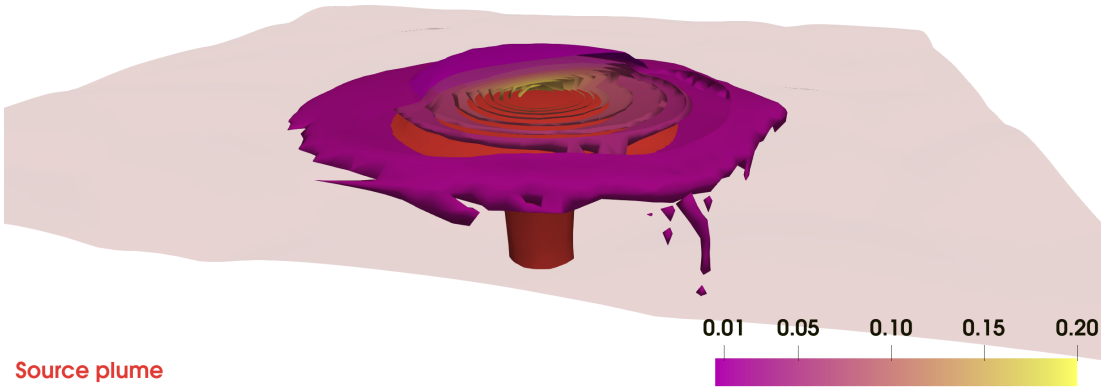


Figure 2.3 A representative convection and melting pattern in the model. We see (a) a typical convection pattern and (b) a typical mantle depletion above the head of the plume, both after 250 My of model evolution.

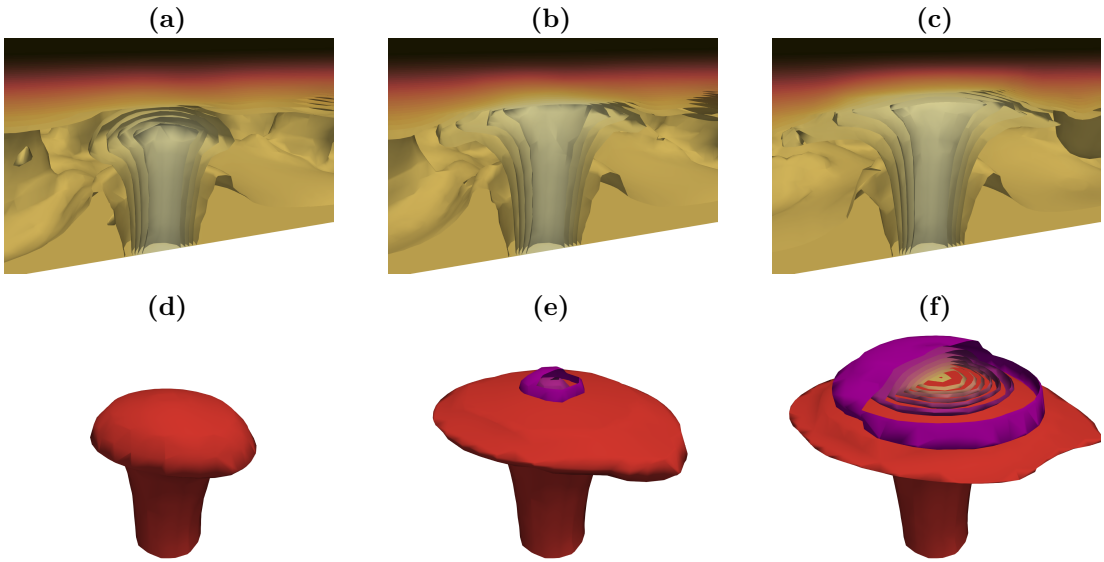


Figure 2.4 A typical model evolution over 100 My: (a-c) a typical plume head evolution and (d-f) a typical mantle depletion evolution.

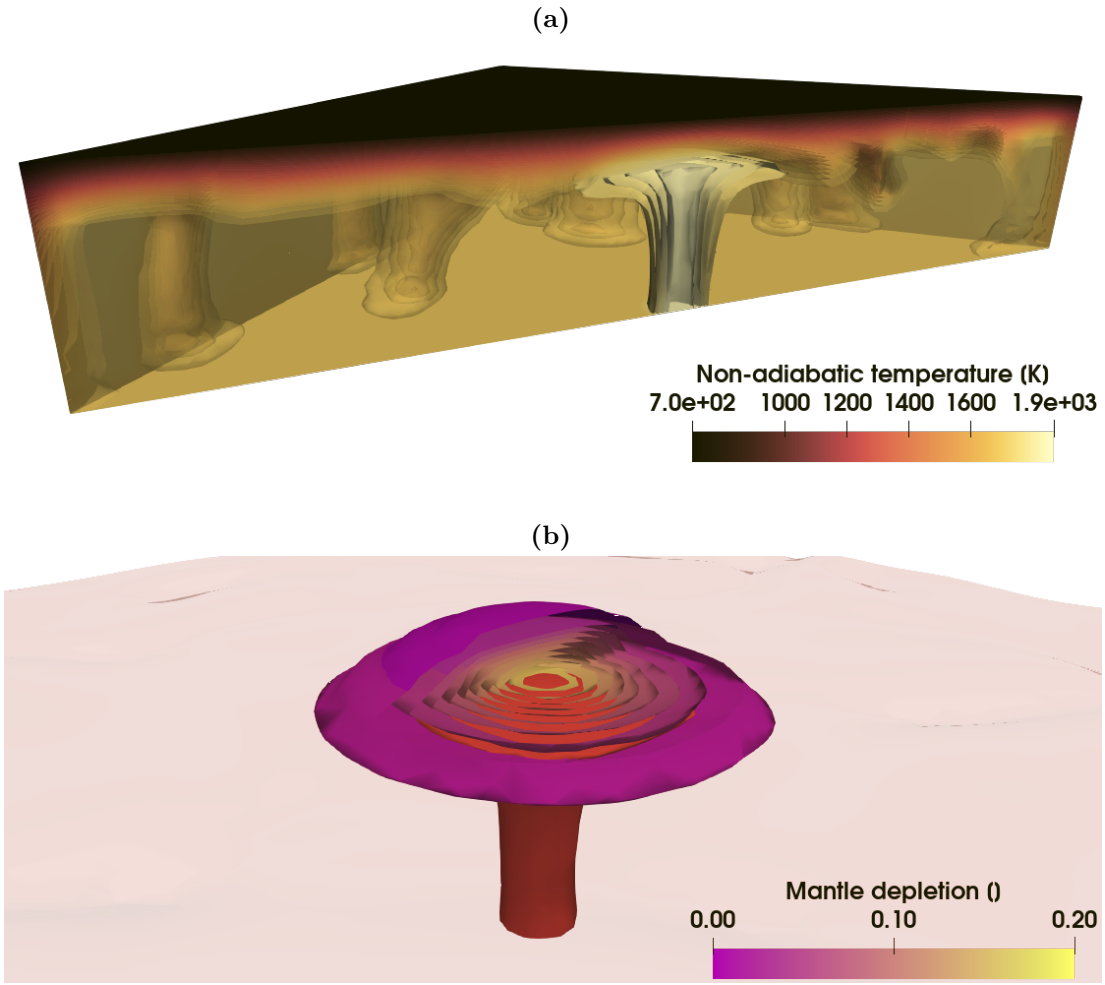


Figure 2.5 The optimal model C2 at 50 My (age from the onset of melting): (a) temperature anomalies in the upper mantle and (b) mantle depletion, i.e. the generated melt.

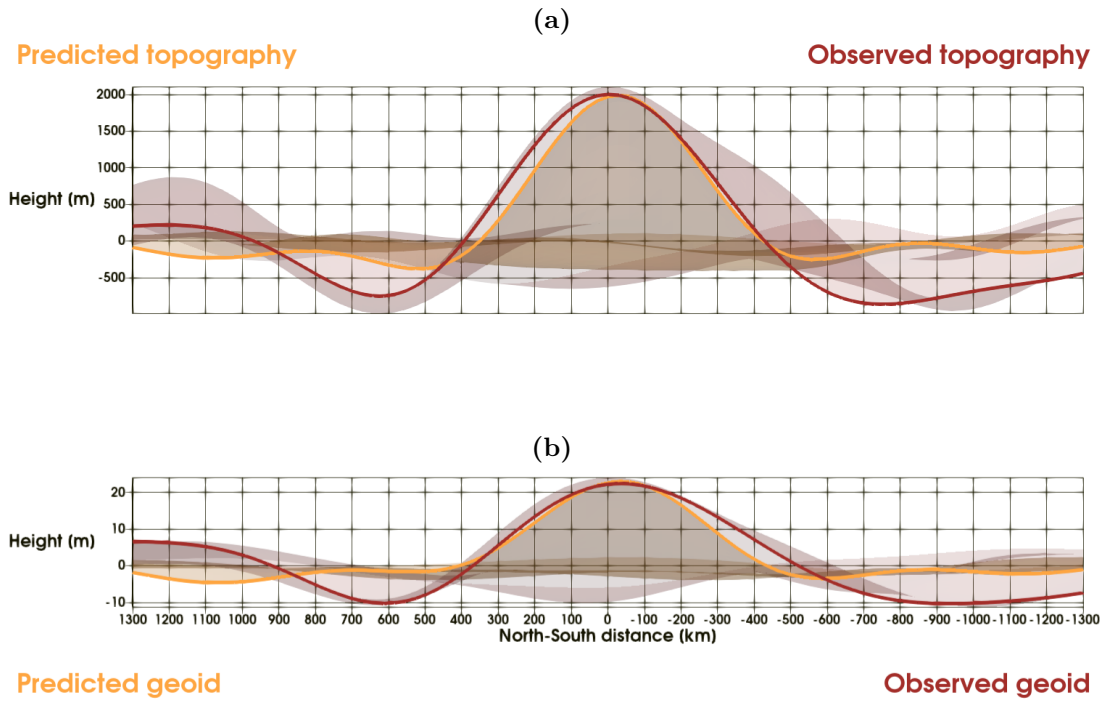


Figure 2.6 The topography and geoid cross section of the optimal model C2 compared to the Ozza Mons data: (a) topography on the degrees 18 to 60, (b) geoid on the degrees 18 to 60. The cross section goes through the topographic peak in the North-South direction. The "shadow" on the graph represents the data from the eastern flank of Ozza Mons (when the cross section is observed from the West side, the "shadow" corresponds to the topography and the geoid behind the volcano).

3 Discussion

As hinted in the previous chapter, our predicted topography is able to reach the observed height and shape of Ozza Mons. Unfortunately, our models strongly underestimate the geoid, as our predicted geoid reaches 50 m but Atla Regio geoid reaches up to 150 m. Some models reveal that increasing elastic and crustal thicknesses leads to a higher geoid, but this effect becomes significant only for unrealistically thick lithosphere and crust. Furthermore, these models lead to a geoid that is high but concentrated around the central topographic peak (as the geoid is generated by the topography, see figure C.5), which is not the case for Atla Regio, as will be shown in the following section.

Our best-fit model consists of a single plume of an approximate width of 200 km and a temperature contrast 150 K. The plume is in the plume head stage and our model shows that first melt eruptions occurred around 50 My ago. Our model predicts the diameter of the plume head to be around 1100 km. The current age and plume head diameter can be compared to geomorphological study of El Bilali et al. (2023). This study concludes that Ozza Mons is currently in a plume head phase. Their analysis of graben systems gives an estimate for the plume head radius of around 1200 km. Based on analogy with Earth's large igneous provinces (LIPs), the age is believed to be less than 50 My. Our model predicts a very similar age (slightly older), however, it also predicts a much smaller plume head than the one inferred from graben analysis. This discrepancy needs to be investigated further and will be the subject of future research.

Comparison of our models to the observed data suggests that Atla Regio is much more complex than we previously assumed and it probably cannot be explained by a simple plume model. Nevertheless, after further inspection of Cytherian surface structures, we believe other volcanic regions are better suited for explanation by our model. These would include Imdr Regio (located around $150°W$ and $45°S$) which is considered to be a site of active volcanism today (López et al., 2024), or Eistla Regio (located at $0°W$ and $20°N$). It seems our approach could be even tested on Beta Regio (located around $75°W$ and $25°N$) as it features high topography and its geoid is highly localized around the topographic peak (unlike Atla Regio's geoid as is discussed in the following section). Nevertheless, Imdr Regio and Eistla Regio are preferred as they are volcanically dominated, whereas Beta Regio is a rift dominated region.

3.1 Interpretation of the geoid

Based on the geoid observed in and around Atla Regio (figure 1), we define three progressively smaller areas that we further discuss:

1. The area with **positive geoid** is very vast as it includes Atla Regio, Ovda Regio, and even Lada Terra. However the area associated only with Atla Regio spans roughly from $30°N$ to $30°S$ and from $165°E$ to $120°W$. Comparing this area to the topographic map we notice that, besides Atla Regio's central volcanic region, this area also includes surrounding rift zones and even lowland plains.

2. The area where the **geoid is higher than 80 m** is already significantly smaller. It is located roughly between $20°N$ and $10°S$, and $170°W$ and $155°W$. Comparison with topography and SAR data shows that this area includes the studied volcanic region as well as other regions, specifically plains north of Maat Mons, and Sapas Mons (another large volcano in the area).

3. The area where the **geoid is higher than 90 m** extents approximatelly from $5°N$ to $5°S$ and from $165°W$ to $155°W$. This area encloses only the central volcanic region (Ozza Mons, Maat Mons, Ongwuti Mons and Uvaysi Mons). Further inspection of the geoid shows presence of two overlapping peaks: one centered at Ozza Mons and one at Maat Mons.

Next, we inspect the topography in these defined areas. We notice that the highest topographic rise in the area (e.g. Maat Mons, Ozza Mons) is predominantly associated with the smallest area where the geoid is higher than 90 m. Our results demonstrate that the proposed scenario (depicted in figure 1.1) explains the small scale features (higher harmonic degrees) of the topography and the geoid associated directly with the central volcanic region[1]. Therefore our results support the idea that Ozza Mons itself was generated by an upwelling.

Besides models with just one plume, during the preliminary phase of 3D modelling we have also tested models with two plumes. These preliminary models suggest that the two-peak nature of the Atla Regio's geoid could be explained by a more complex plume (see figure C.4), maybe a scenario similar to the one El Bilali et al. (2023) describe in their work. When we compare the geoid to the topography of Maat Mons and Ozza Mons, we notice geoid signals are similar, but the topography differs strongly. Maat Mons' topography is both much higher and more localized than the topography of Ozza Mons. We believe the differences in the topography may be attributed to the melt transport mechanisms acting differently in each Mons. The SAR imagery shows that the area covered by volcanic edifices and pits is much larger at Ozza Mons' summit than Maat Mons'. The analysis of volcanoes' graben systems reveals a more extensive sills system beneath Ozza Mons (El Bilali et al., 2023), which indicate a different melt behaviour in the crust. Sill intrusions distribute magma laterally, creating wider but lower edifices compared to vertical dikes. This could potentially lead to the pronounced dissimilarity in the topography of the two peaks.

Our limited capability to predict the geoid of the rest of the region indicates that the mantle structure beneath Atla Regio (and possibly the whole BAT region) is much more complex than the proposed simple plume. We can speculate that some effects that are not included in our approach may be at play.

As is revealed, the Regio uplift is a highly complicated process and we are not able to provide a complete picture of the system behaviour due to time constraints. Before we carry out a systematic 3D study of uplift scenarios, we propose improvements of the current approach based on difficulties we faced during our work.

[1] As shown by model C2, see figure 2.6

3.2 Further model development

Below we present a list of possible enhancements of our models. These could improve the long-wavelength geoid predictions and include new effects and offer additional geomorphological predictions.

1. **Sublithospheric plume spreading**. A significant spreading of the plume beneath the lithosphere is observed in some of our 3D models, specifically those with low upper mantle viscosity and high plume temperature (see figure C.2). In our case, the side boundaries artificially stop the spreading of the plume, suggesting the plume could spread even further if the boundaries were further away. Such a widespread buoyant thermal anomaly just beneath the lithosphere could generate a long wavelength dynamic topography and therefore a high geoid (J. Maia, personal communication, June 18, 2025). On the other hand, the melting pattern, which is caused by the spreading plume, is not as localized as is expected based on the data available in the region. Geoid inversion models (Maia et al., 2023; Pauer et al., 2006) indicate a presence of a low viscosity layer just beneath the lithosphere. We hypothesise this layer forms through the presence of a partially molten plume material. This scenario needs to be investigated further.

2. **Coupling with lower mantle dynamics**. Inclusion of the lower mantle in ASPECT calculations would enable generation of mantle plumes consistent with the global mantle structure. Additionally, the gravitational effects of the lower mantle loads could be calculated directly, eliminating any need to supply a parametric model of the lower mantle plume into the model. Furthermore, such improvement could directly incorporate large scale lower mantle structures (similar to Earth's megaplumes) and explore their potential effect on the predicted values. Perhaps, this could quantitatively explain the long wavelength geoid.

3. **Effect of magmatic intrusions**. Our current model assumes Venus (or at least Atla Regio) operates in an episodic lid regime which is simulated via high cohesion that leads to a thick and mature lithosphere. However, recently there is a growing consensus in the community that Venus is in a plutonic squishy lid regime. Incorporating the effects of heat transport due to magmatic intrusions would enable simulating the lithosphere of a plutonic squishy lid regime. Including this effect would require significant modifications to the solved equations, as discussed in the following section. This effect was so far studied only on a global scale (Lourenço et al., 2020) and requires further investigation for our case.

4. **Calculating lithospheric stresses**. Currently we compare our predictions only to the observed topography and geoid. However, the largest dataset available today is the SAR imagery, which reveals a large number of rifts in and around Atla Regio. We expect that our model will not be able to predict large scale rifts such as Devana or Parga Chasmata. But, comparing the surface stress field generated by our model to the observed rifting could further hint at possible internal structure of the area and provide additional constraints (A. Gülcher, personal communication, April 29, 2025). If we

indeed demonstrate that our model cannot predict large scale rifting areas, that would suggest that there are other long wavelength stress sources beyond our model's framework.

5. **Realistic dynamic topography**. The final enhancement involves implementing realistic dynamic topography. In the current approach, we model the dynamic topography through the vertical traction of the free slip boundary condition. This formulation neglects the time required to build the topography and therefore any stress variations induce instantaneous topographic responses. Realistic modelling of the dynamic topography could be achieved by prescribing a free surface boundary condition at the top boundary. This could lead to significant changes in the computed geoid and topography, which could further help determine the current stage of the plume developement beneath Atla Regio.

At the current stage of our project, the first improvement should be the inclusion of the free surface boundary condition, as it is already implemented in ASPECT and the changes in the predicted geoid might be significant. Also, calculating the surface stresses should not pose a substantial obstacle as it only requires standard postprocessing. At the next stage, the model can be expanded to the lower mantle which would provide a self-consistent mantle plume. This requires slight changes in the rheology, specifically implementation of the pressure dependent diffusion creep and perhaps inclusion of phase transitions. Further research, specifically spreading plume scenario and inclusion of intrusions, requires more significant modifications to the current approach, predominantly concerning the melt treatment.

3.3 Current limitations of the model

3.3.1 Melting model

The closely followed approach of Capitanio et al. (2024) utilizes the simplified empirical melting model of McKenzie and Bickle (1988). It was developed to describe the decompression melting appearing beneath the Earth's mid-ocean ridges. This melting model is still applicable in our case as the rising plume also causes decompression melting of the mantle material, but the simplifications lead to potential problems:

1. We calculate the crustal topography by vertical integration of the mantle depletion during the postprocessor phase. As a result, lateral movement of a depleted area results in a lateral movement of the observed topography. In the case of Capitanio et al. (2024) this effect is physically valid as long as depleted areas that produced the extruded melt are a part of the lithosphere (or are in the near proximity). If they are, the lateral movement of the surface is coupled with the movement of the depleted area and therefore the topography should in reality stay above the melting source (i.e. topography should move together with the depleted area). In our case, the mantle plume causes additional movements of the depleted areas beneath the lithosphere that are not coupled to the movements of the surface. This leads to our

model showing lateral movement of the crustal topography, while in reality no movement should be present. Our estimates of the lateral movement of the depleted areas show maximum displacement of around 70 km throughout the model evolution. This effect is most significant in the areas of low mantle depletion.

2. Another potential problem in our approach is the vertical transport of melt. We assume that, once melting occurs, the melt is immediately transported to the surface. As illustrated in figure 3.1, a simple melt extraction mechanism violates the continuity equation due to the mass being transported to the surface. Theoretical examination of this issue reveals that if we consider the melt to be isostatically compensated immediately after extrusion, the void left behind by the melt after it's extraction is perfectly filled by the volume of the crustal root associated with the isostatic compensation of the extruded melt. If, as in our case, the compensation is not isostatic but rather elastic, the crustal root volume is slightly smaller than the empty volume left behind by the melt.We assume the rest of the empty volume is filled by an influx of the material from the rising mantle plume below. However, for both compensation mechanisms we assume immediate compensation of the crustal topography, which could be a significant simplification.

In order to decouple the movement of the crustal topography and melting source, and to model its realistic relaxation (so that no assumption of immediate isostasy is needed), we need to include source terms in continuity and heat transport equations (and perhaps even in the momentum equation). Melt leaving the element where it was generated would be modelled as a negative source of mass and heat, intrusions would be modelled as positive sources of mass and heat in the crust and extrusions as an additional vertical displacement of the free boundary at the top of the model domain. The implementation of this mechanism will be quite complicated as we will need to implement non-local effects in the finite elements code. However, this approach would self-consistently model the melt transport and the problems that we discuss in this section would not appear.

3.3.2 Lateral lava mobility

The lateral lava mobility is yet another unmodelled effect that requires our further discussion. In our approach, we assume that lavas stay in place after their extrusion and do not move laterally over any significant distances. This assumption does not have to be valid, as even a small topographic slope is able to make a basaltic lava flow far away (D. Gerritsen, personal communication, May 2, 2025). Inspection of the Cytherian surface reveals a large number of lava flows exceeding hundreds of kilometers, some even originating from impact craters. This indicates that the lateral movement of unsolidified lavas could have a substantial effect on the final surface distribution of the extruded material (and therefore on the shape and height of the crustal topography).

Based on the lava mobility, there are two main possible scenarios of a Regio uplift, both scenarios are illustrated in figure 3.2. The static lava scenario causes the melt extrusions to increase the total topography, while the mobile lava scenario cause a decrease in the total topography. Additionally, if we were

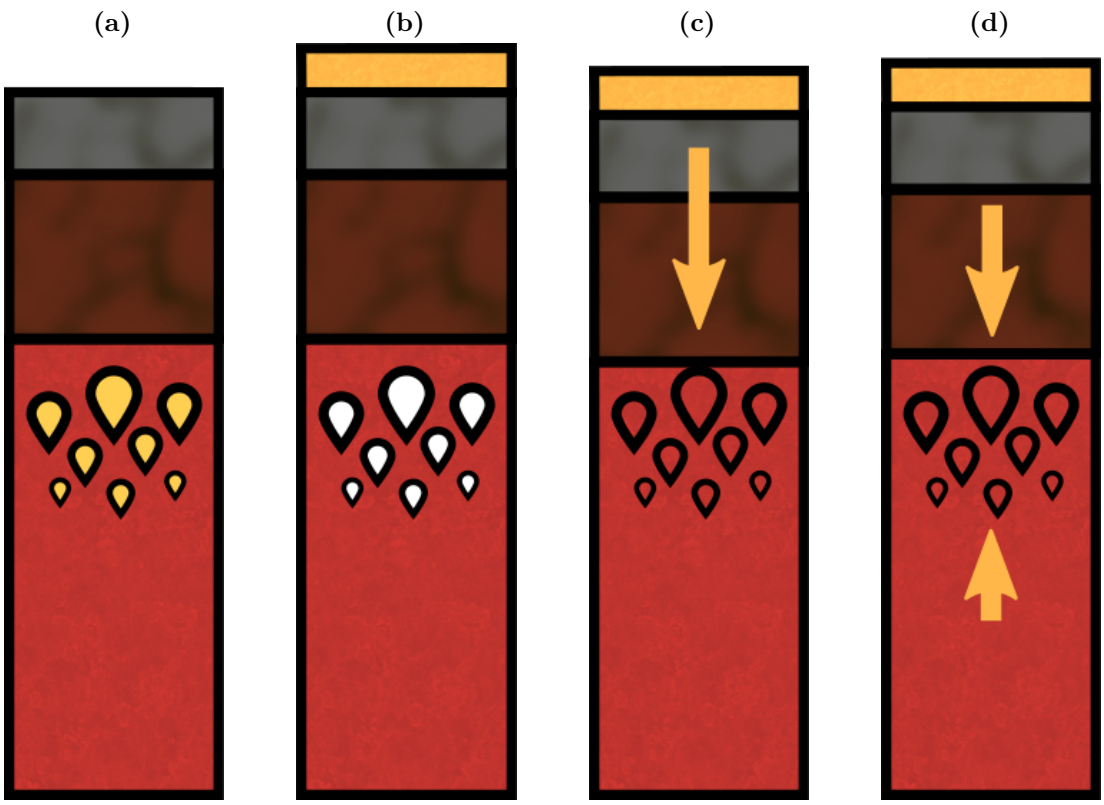


Figure 3.1 An illustration of our current melt extraction approach: (a) a mantle pillar with partially molten material (orange droplets), (b) the melt is extracted to the surface (orange layer on top) and leaves behind an unfilled space (white droplets). This void is filled by mantle material either (c) from the top only, which corresponds to an immediate isostastic compensation of the crustal topography, or, as in our case, (d) both from the top and slightly from the bottom, which corresponds to the elastic compensation. Arrows represent material transport directions.

to investigate possible sites of a Regio collapse (e.g. Laufey Regio), the lava mobility scenario plays an important role in the final topography of a collapsed Regio, as it determines the crustal thickness in and surrounding the Regio.

In the context of the Earth, a rising plume that generates melt under the lithosphere leads to the formation of a LIP as shown by Farnetani and Richards (2025). Investigation of the Earth's LIPs, where the dynamic topography has already vanished, allows us to distinguish between the two presented scenarios. An examination of Siberian Traps (or Deccan Traps) reveals that the remanent topography of a LIP is significant and therefore aligns more with the static lava scenario. Nevertheless, there are also opposite cases, such as Yellowstone national park, where the present day topography resembles the second scenario, i.e. the mobile lavas scenario (Gerritsen et al., 2025). Numerical studies of the lava flow under the Cytherian conditions result in a 75% increase in the flow length compared to the Earth (Flynn et al., 2023). However, as many Cytherian volcanoes (including Ozza Mons) exhibit lava flows that do not extend beyond the topographic rise significantly, we believe our approach is valid on the current level of model complexity.

Unfortunately, there is no straightforward way to include the effects of surface lava mobility in our model self-consistently. This issue requires further examination

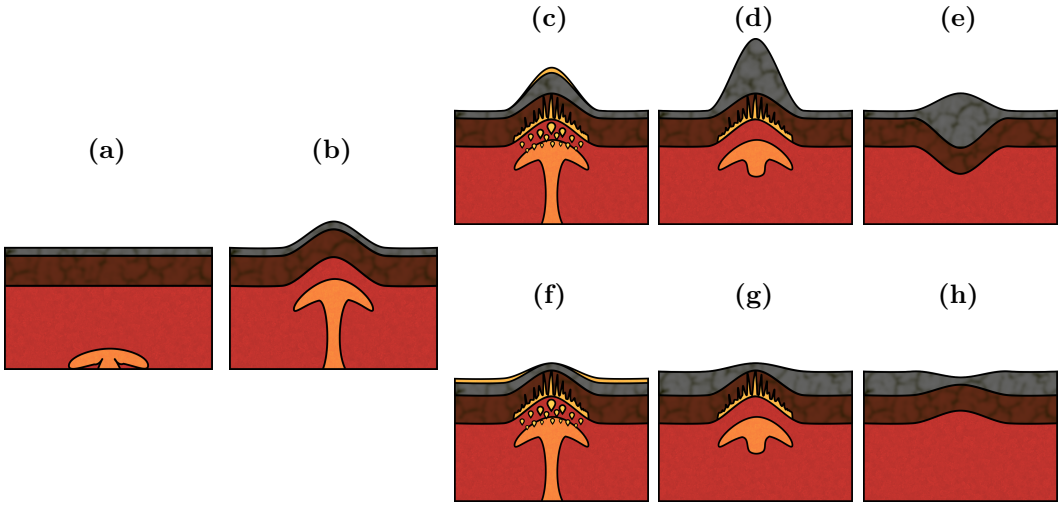


Figure 3.2 Two possible evolutionary paths of a Regio uplift depending on surface lava mobility. In the beginning of our Regio formation scenario, (a) the mantle plume slowly develops and (b) causes the uplift of the dynamic topography. Once melting occurs, there are two endmembers of the ongoing process of Regio formation: either (c-e) the lava stays at the eruption sites, i.e. is static, or (f-h) the lava flows downwards based on the current slope of the total topography, i.e. is mobile. In the case of (e) static lava the crustal topography tends to isostasy and the higher crustal thickness in the Regio preserves some remanent topography, even after the loss of dynamic support. On the other hand, if (h) the lava is mobile a local depression is formed as in this case the crustal thickness is smaller inside the Regio, compared to Regio's surroundings.

and perhaps will be a subject of a future study.

3.3.3 Mantle rheology

So far, our mantle rheology model includes only the temperature dependent diffusion creep (diffusion activation volume is equal to zero). In the case of the upper mantle, the temperature variations have a greater effect on the viscosity than pressure variations. Thus the pressure dependence of the diffusion creep can be omitted, leaving only the temperature dependence. However, if the lower mantle is to be added to the model, the pressure dependence cannot be omitted as it is the primary cause of the viscosity increase in the lower mantle that is observed by the geoid inversion studies.

Another important creep mechanism that we need to include in our model in the future, is the dislocation creep which predominantly acts in regions of high strain-rate. In our case, this mechanism could play an important role in the area around the plume head where it spreads beneath the lithosphere. Similarly, including viscous heating in our model would cause additional heating in regions of high viscosity and strain-rate. This could further decrease viscosity (and increase strain-rate) in the plume and perhaps even become a heat source leading to more melting in the region.

In some models, the Earth's asthenospheric viscosity drop is explained by the presence of a partially molten rock which extrudes to the surface only once it reaches a given threshold. Even a small amount of this melt trapped in the host rock decreases the viscosity (Holtzman, 2016). Implementation of this mechanism

could reduce the viscosity of the plume material that is spread beneath the lithosphere as our models already predict presence of partial melting in that region. We can even speculate that it could cause further spreading of the plume and help explain the possible asthenosphere-like viscosity drop as observed in geoid inversion studies. Moreover, the presence of a lower density melt could decrease the effective density of the plume material which would help build the dynamic topography and explain the long wavelength geoid.

Implementation of the pressure dependent diffusion creep as well as the dislocation creep does not pose a significant challenge, since these creep mechanisms are already implemented in ASPECT. However, adding these creep mechanisms increases the total number of material parameters which are largely unknown for Venus, and therefore we would have to further rely on the analogy with the Earth. Implementation of viscous heating does not seem to be a technically challenging either. But, if we were to include this effect, we would also need to improve our current approach to adiabatic heating, as well as latent heat of melting. Improving the approach to these two effects is problematic in the current stage of model development and would most certainly require a different model of melting.

Conclusion

In this work we have developed a model of Atla Regio uplift including melting effects. A series of 2D and 3D models was carried out that gave us an insight into the plume and melting behaviours. Moreover, a best-fit model for higher degrees of topography and geoid was developed and compared with geomorphological studies. Below we list conclusions that can be made based on our work.

1. Our approach, despite its current limitations, is able to predict the topography and the geoid of Atla Regio for harmonic degrees between 18 and 60.

2. The inferred plume temperature variation is approximately 150 K, with the plume width of about 200 km and plume head width around 1100 km.

3. The inferred age of Atla Regio is around 50 My.

4. Ozza Mons has overall produced around 2 million km^3 of melt.

5. Modelling in 2D leads to ridging effects, therefore 3D modelling is required.

6. Since Atla Regio is a complex region with many intertwined effects at play, a simple mantle plume model cannot explain the large geoid elevation at low harmonic degrees. As a parametric model of the lower mantle plume cannot explain the large scale geoid, either more complex lower mantle model is required, or it is necessary to include additional effects in the upper mantle, or both.

Bibliography

Armann, Marina and Paul J. Tackley (Dec. 2012). "Simulating the thermo-chemical magmatic and tectonic evolution of Venus's mantle and lithosphere: Two-dimensional models". en. In: *Journal of Geophysical Research: Planets* 117.E12. DOI: 10.1029/2012je004231. URL: http://dx.doi.org/10.1029/2012JE004231.

Bangerth, Wolfgang et al. (2023). *geodynamics/aspect: ASPECT 2.5.0*. Zenodo. DOI: 10.5281/ZENODO.8200213. URL: https://zenodo.org/record/8200213.

Brossier, J. et al. (Mar. 2021). "Distinct Mineralogy and Age of Individual Lava Flows in Atla Regio, Venus Derived From Magellan Radar Emissivity". en. In: *Journal of Geophysical Research: Planets* 126.3. DOI: 10.1029/2020je006722. URL: http://dx.doi.org/10.1029/2020JE006722.

Byrne, Paul K. et al. (2021). "A globally fragmented and mobile lithosphere on Venus". en. In: *Proceedings of the National Academy of Sciences* 118.26. DOI: 10.1073/pnas.2025919118. URL: http://dx.doi.org/10.1073/pnas.2025919118.

Capitanio, Fabio A. et al. (Aug. 2024). "Ishtar Terra highlands on Venus raised by craton-like formation mechanisms". en. In: *Nature Geoscience* 17.8, pp. 740–746. DOI: 10.1038/s41561-024-01485-3. URL: http://dx.doi.org/10.1038/s41561-024-01485-3.

El Bilali, Hafida et al. (2023). "Dyke swarms record the plume stage evolution of the Atla Regio superplume on Venus". en. In: *Communications Earth amp; Environment* 4.1. DOI: 10.1038/s43247-023-00901-7. URL: http://dx.doi.org/10.1038/s43247-023-00901-7.

Farnetani, Cinzia G. and Mark A. Richards (Mar. 2025). *The origin of carbonatite magmas predating main-phase LIPs eruptions*. DOI: 10.5194/egusphere-egu25-16266. URL: http://dx.doi.org/10.5194/egusphere-egu25-16266.

Flynn, Ian. T. W., Magdalena. O. Chevrel, and Michael. S. Ramsey (2023). "Adaptation of a Thermorheological Lava Flow Model for Venus Conditions". en. In: *Journal of Geophysical Research: Planets* 128.7. DOI: 10.1029/2022je007710. URL: http://dx.doi.org/10.1029/2022JE007710.

Foster, Adrian and Francis Nimmo (1996). "Comparisons between the rift systems of East Africa, Earth and Beta Regio, Venus". en. In: *Earth and Planetary Science Letters* 143.1–4, pp. 183–195. DOI: 10.1016/0012-821x(96)00146-x. URL: http://dx.doi.org/10.1016/0012-821X(96)00146-X.

Garvin, James B. et al. (May 2022). "Revealing the Mysteries of Venus: The DAVINCI Mission". In: *The Planetary Science Journal* 3.5, p. 117. DOI: 10.3847/psj/ac63c2. URL: http://dx.doi.org/10.3847/PSJ/ac63c2.

Gerritsen, Dieke et al. (Mar. 2025). *Magnetic tracing of lost time in Cenozoic sediments: Testing dynamic topography of the Yellowstone plume, USA*. DOI: 10.5194/egusphere-egu25-3202. URL: http://dx.doi.org/10.5194/egusphere-egu25-3202.

Ghail, Richard C. et al. (Feb. 2018). "VenSAR on EnVision: Taking earth observation radar to Venus". en. In: *International Journal of Applied Earth Observation*

and Geoinformation 64, pp. 365–376. DOI: 10.1016/j.jag.2017.02.008. URL: http://dx.doi.org/10.1016/j.jag.2017.02.008.

Ghail, Richard C. et al. (Apr. 2024). "Volcanic and Tectonic Constraints on the Evolution of Venus". en. In: *Space Science Reviews* 220.4. DOI: 10.1007/s11214-024-01065-2. URL: http://dx.doi.org/10.1007/s11214-024-01065-2.

Heister, Timo et al. (May 2017). "High accuracy mantle convection simulation through modern numerical methods – II: realistic models and problems". en. In: *Geophysical Journal International* 210.2, pp. 833–851. DOI: 10.1093/gji/ggx195. URL: http://dx.doi.org/10.1093/gji/ggx195.

Holtzman, Benjamin K. (Feb. 2016). "Questions on the existence, persistence, and mechanical effects of a very small melt fraction in the asthenosphere". en. In: *Geochemistry, Geophysics, Geosystems* 17.2, pp. 470–484. DOI: 10.1002/2015gc006102. URL: http://dx.doi.org/10.1002/2015GC006102.

Ivanov, M. A. and J. W. Head (Oct. 2011). "Global geological map of Venus". en. In: *Planetary and Space Science* 59.13, pp. 1559–1600. DOI: 10.1016/j.pss.2011.07.008. URL: http://dx.doi.org/10.1016/j.pss.2011.07.008.

Ivanov, M. A., J. W. Head, and A. T. Basilevsky (Jan. 2015). "History of the long-wavelength topography of Venus". en. In: *Solar System Research* 49.1, pp. 1–11. DOI: 10.1134/s0038094615010025. URL: http://dx.doi.org/10.1134/S0038094615010025.

James, Peter B., Maria T. Zuber, and Roger J. Phillips (Apr. 2013). "Crustal thickness and support of topography on Venus". en. In: *Journal of Geophysical Research: Planets* 118.4, pp. 859–875. DOI: 10.1029/2012je004237. URL: http://dx.doi.org/10.1029/2012JE004237.

Johnson, W.T.K. (1991). "Magellan imaging radar mission to Venus". In: *Proceedings of the IEEE* 79.6, pp. 777–790. DOI: 10.1109/5.90157. URL: http://dx.doi.org/10.1109/5.90157.

Katz, Richard F., Marc Spiegelman, and Charles H. Langmuir (2003). "A new parameterization of hydrous mantle melting". en. In: *Geochemistry, Geophysics, Geosystems* 4.9. DOI: 10.1029/2002gc000433. URL: http://dx.doi.org/10.1029/2002GC000433.

Konopliv, A.S., W.B. Banerdt, and W.L. Sjogren (May 1999). "Venus Gravity: 180th Degree and Order Model". en. In: *Icarus* 139.1, pp. 3–18. DOI: 10.1006/icar.1999.6086. URL: http://dx.doi.org/10.1006/icar.1999.6086.

Kronbichler, Martin, Timo Heister, and Wolfgang Bangerth (Aug. 2012). "High accuracy mantle convection simulation through modern numerical methods". en. In: *Geophysical Journal International* 191.1, pp. 12–29. DOI: 10.1111/j.1365-246x.2012.05609.x. URL: http://dx.doi.org/10.1111/j.1365-246X.2012.05609.x.

López, I. et al. (Oct. 2024). "Geologic Evolution of Imdr Regio, Venus: Insight Into the Origin of a Possible Young/Active Hot Spot". en. In: *Journal of Geophysical Research: Planets* 129.10. DOI: 10.1029/2024je008604. URL: http://dx.doi.org/10.1029/2024JE008604.

Lourenço, Diogo L. et al. (Apr. 2020). "Plutonic-Squishy Lid: A New Global Tectonic Regime Generated by Intrusive Magmatism on Earth-Like Planets". en. In: *Geochemistry, Geophysics, Geosystems* 21.4. DOI: 10.1029/2019gc008756. URL: http://dx.doi.org/10.1029/2019GC008756.

Maia, J. S., M. A. Wieczorek, and A.-C. Plesa (2023). "The Mantle Viscosity Structure of Venus". en. In: *Geophysical Research Letters* 50.15. DOI: 10.1029/2023gl103847. URL: http://dx.doi.org/10.1029/2023GL103847.

McKenzie, D. and M. J. Bickle (1988). "The Volume and Composition of Melt Generated by Extension of the Lithosphere". en. In: *Journal of Petrology* 29.3, pp. 625–679. DOI: 10.1093/petrology/29.3.625. URL: http://dx.doi.org/10.1093/petrology/29.3.625.

Pauer, M., K. Fleming, and O. Čadek (Nov. 2006). "Modeling the dynamic component of the geoid and topography of Venus". en. In: *Journal of Geophysical Research: Planets* 111.E11. DOI: 10.1029/2005je002511. URL: http://dx.doi.org/10.1029/2005JE002511.

Rappaport, Nicole J. et al. (May 1999). "An Improved 360 Degree and Order Model of Venus Topography". en. In: *Icarus* 139.1, pp. 19–31. DOI: 10.1006/icar.1999.6081. URL: http://dx.doi.org/10.1006/icar.1999.6081.

Rosenblatt, P., P. C. Pinet, and E. Thouvenot (Mar. 1994). "Comparative hypsometric analysis of Earth and Venus". en. In: *Geophysical Research Letters* 21.6, pp. 465–468. DOI: 10.1029/94gl00419. URL: http://dx.doi.org/10.1029/94GL00419.

Smrekar, Sue et al. (Mar. 2022). *VERITAS (Venus Emissivity, Radio Science, InSAR, Topography, and Spectroscopy): A Discovery Mission*. DOI: 10.1109/aero53065.2022.9843269. URL: http://dx.doi.org/10.1109/AERO53065.2022.9843269.

Strom, Robert G., Gerald G. Schaber, and Douglas D. Dawson (May 1994). "The global resurfacing of Venus". en. In: *Journal of Geophysical Research: Planets* 99.E5, pp. 10899–10926. DOI: 10.1029/94je00388. URL: http://dx.doi.org/10.1029/94JE00388.

Svedhem, H. et al. (Mar. 2009). "Venus Express mission". en. In: *Journal of Geophysical Research: Planets* 114.E5. DOI: 10.1029/2008je003290. URL: http://dx.doi.org/10.1029/2008JE003290.

Turcotte, D. L. et al. (May 1981). "Role of membrane stresses in the support of planetary topography". en. In: *Journal of Geophysical Research: Solid Earth* 86.B5, pp. 3951–3959. DOI: 10.1029/jb086ib05p03951. URL: http://dx.doi.org/10.1029/JB086iB05p03951.

Vezolainen, A. V. et al. (Aug. 2004). "Uplift of Beta Regio: Three-dimensional models". en. In: *Journal of Geophysical Research: Planets* 109.E8. DOI: 10.1029/2004je002259. URL: http://dx.doi.org/10.1029/2004JE002259.

List of Figures

1 Global topography and geoid 8
2 Atla Regio topography and geoid 10

1.1 Proposed scenario of Regio uplift 11
1.2 Illustration of the upper and lower mantle dynamics 16

2.1 Total heat flux and RMS velocity for different tectonic regimes . . 22
2.2 Evolution of melting in a 2D model 24
2.3 Representative convection and melting pattern in a 3D model . . 28
2.4 A typical model evolution over 100 My 29
2.5 The optimal model C2 at 50 My 29
2.6 The topography and geoid cross section of the optimal model C2 compared to the Ozza Mons data 30

3.1 An illustration of our approach to melt extraction 36
3.2 Effect of surface lava mobility on the evolution of Regio uplift . . 37

C.1 Topography and convection of model A 54
C.2 Topography and convection of model B 55
C.3 Topography and convection of model C 56
C.4 Topography and convection of model CCH-2 56
C.5 Topography and geoid of model C2e2 57

List of Tables

1.1 Considered density anomalies when calculating the geoid. 18

2.1 Material parameters 20
2.2 Individual tested models during the minimization. 27

B.1 Material parameters for model IM-A 50
B.2 Initial models parameter changes 51
B.3 2D Regio models with thermal variations 51
B.4 2D Regio models with variations in plume width and activity time 52
B.5 2D Regio models with fixed plume and varied mantle material parameters 53

List of Abbreviations

Abbreviation	Definition
t	time
r	radius
T	temperature
T_n	non-adiabatic temperature
T_{nr}	non-adiabatic radial temperature
T_{sol}	solidus temperature
T_{liq}	liquidus temperature
$\vec{v}$	velocity vector
$\dot{\mathbf{e}}$	strain-rate
p'	pressure variation
p	pressure
Φ	potential mantle depletion
F	mantle depletion
d	depth
ρ_r	radially varying density
ρ	density
$\Delta\rho$	density varition
ρ_0	reference density
α	thermal expansivity
c_p	specific heat capacity
k	thermal conductivity
g	gravity
G	gravitational constant
$\vec{g}$	gravity vector
h	internal heat source density
T_{ss}	melt parametric temperature
$\delta\rho_F$	density change due to mantle depletion
A^{diff}	diffusion prefactor
E_a^{diff}	diffusion activation energy
R	molar gas constant
K	water partition coefficient
δT_F	latent heat (temperature equivalent)
η	viscosity
η_0	reference viscosity
η_{min}	minimum viscosity
η_{max}	maximum viscosity
$\vec{e}_z$	vertical unit vector
$\vec{e}_r$	radial unit vector
C	cohesion
δC_F	cohesion change due to depletion
μ	friction coefficient
$\delta\mu_F$	friction coefficient change due to depletion
$\dot{e}_{II}^D$	second invariant of deviatoric strain rate
$\mathbf{t}$	Cauchy stress tensor

Abbreviation	Definition
$\mathbf{t}_{\mathrm{LM}}$	Cauchy stress tensor in the lower mantle
$\mathbf{t}_{\mathrm{UM}}$	Cauchy stress tensor in the upper mantle
η_{upp}	upper mantle viscosity for the lower mantle model
η_{low}	lower mantle viscosity for the lower mantle model
S_{U}	upper mantle plume source area
r_{L}	lower mantle plume radius
ρ_{K}	core density
t_{f}	total topography
t_{obs}	observed topography
t_{D}	dynamic topography (top)
$t_{\mathrm{D}}^{(b)}$	dynamic topography (bottom)
t_{C}	crustal topography
d_{C}	crustal thickness
d_{ADC}	apparent depth of compensation
ρ_{C}	crustal density
C_l	compensation coefficient of elastic flexure
R	Venus radius
R_{730}	phase transition radius
R_{CMB}	core-mantle boundary radius
$h_{\mathrm{C}}^{(t)}$	geoid contribution: crustal surface topography
$h_{\mathrm{C}}^{(r)}$	geoid contribution: crustal root topography
$h_{\mathrm{D}}^{(t)}$	geoid contribution: dynamic topography
$h_{\mathrm{D}}^{(b)}$	geoid contribution: dynamic topography on the CMB
h_{UM}	geoid contribution: upper mantle density variations
h_{LM}	geoid contribution: lower mantle density variations
h_{t}	total modelled geoid
h_{obs}	observed geoid
l	spherical harmonic degree
Y_{lm}	spherical harmonic function
L	misfit function
f_{Ozza}	Ozza Mons filter
f_{Maat}	Maat Mons filter
$\hat{f}_{\mathrm{SH}}(l)$	spectral filter at degree l
F_{tg}	geoid scale factor

A Topography, Gravity, and Geomorphology of Venus

The work of Ghail et al. (2024) is the main source for this appendix.

A.1 Available Data

Due to Venus's dense and opaque atmosphere, direct optical imaging of its surface is impossible. However, different datasets were obtained through alternative methods. The available data include topographic and gravity measurements up to spherical harmonic degree 360, as well as emissivity data and synthetic aperture radar (SAR) imagery from both left- and right-looking observations. These radar images provide detailed views of Venus's surface in the microwave spectrum. Additionally, surface photographs from some of the landers are available and emissivity data have later been obtained for the southern hemisphere in infrared spectrum.

Venus's topography can be broadly categorized into two main regions: highlands and lowlands. Unlike Earth's distinct separation between oceanic seafloor and continental landmasses, Venus's highland regions occupy a much smaller portion of the surface and generally lack extensive flat plateaus. This difference is evident in comparative hypsometry studies of the two planets (Rosenblatt et al., 1994). The most prominent highlands on Venus include Ishtar Terra, Ovda Regio, Thetis Regio, Atla Regio, and Beta Regio, among others.

Gravity anomalies on Venus similarly exhibit a weak dichotomy, reflecting the division between highlands and lowlands. When correlated and uncorrelated gravity anomalies are analyzed, a notable distinction emerges among the highlands. Some highland regions, such as Ishtar Terra, Ovda Regio, and Thetis Regio, exhibit negative uncorrelated gravity anomalies, suggesting the presence of significant crustal roots and partial isostatic compensation. In contrast, other highlands, such as Atla Regio, Beta Regio, and Lada Terra, exhibit positive uncorrelated gravity anomalies, indicating a different lithospheric structure, potentially lacking deep crustal roots or having high dynamic topography.

Similar classification of Venus's surface is revealed based on SAR imaging (Ivanov and Head, 2011), here we provide a brief overview of geomorphology of already defined region types. The most common geomorphological units include regional plains (40.3%), shield plains (17.4%), lobate plains (8.3%), groove belts (8.1%), and tessera terrains (7.3%). A short overview of these terrains is given below:

1. Regional and shield plains: These units, the most abundant on Venus, predominantly cover lowland regions. They are characterized by smooth surfaces, often punctuated by small volcanic edifices.

2. Lobate plains: Found mainly in Lada Terra, Atla Regio, Beta Regio, and Thetis Regio. These regions display a distinctive non-uniform albedo pattern, with dark, flow-like features indicative of volcanic activity and large lava flows. Many of these areas are associated with large volcanoes.

3. Tessera terrains: Primarily located in Ishtar Terra, Ovda Regio, and Thetis Regio, tessera terrains represent Venus's most deformed landscapes, exhibiting complex tectonic features.

A.2 Tectonic Regime of Venus

Analysis of available data suggests that Venus's surface can be categorized into three primary terrain types: tessera highlands, lobate plains highlands, and lowlands. The geologic history inferred from deformation patterns in tessera terrains, the distribution of lowland plains surrounding them, and impact crater statistics suggests a possible evolutionary sequence for Venus's surface.

The oldest terrains on Venus are the tessera highlands, which formed prior to a hypothesized global resurfacing event and are classified as pre-Guineverian. The lowland plains, including Guinevere and Rusalka Planitia, are believed to have formed during this resurfacing event and correspond to the Guineverian/Atlian period. The youngest units, the lobate plains highlands, represent the most recent volcanic activity on Venus. Several hypotheses have been proposed to explain Venus's current tectonic regime:

1. Global episodic lid regime: This model suggests that Venus undergoes periodic episodes of lithospheric overturn, with long quiescent periods in between. This regime requires intermediate and high extrusion rates and intermediate cohesion values (Armann and Tackley, 2012). If this hypothesis is correct, Venus is currently in a stable phase, with a single mature lithospheric lid. The last global resurfacing event likely occurred between 300 and 700 million years ago (Strom et al., 1994), meaning that Venus's lithosphere has had ample time to mature since.

2. Plutonic squishy lid regime: An alternative hypothesis, that is quite popular recently, proposes that Venus's lithosphere is fragmented into smaller blocks due to high rates of magmatic intrusion and moderate to high lithospheric cohesion (Lourenço et al., 2020). This hypothesis could be supported by observations of disrupted lowland regions that appear segmented into crustal blocks (Byrne et al., 2021).

In this thesis, we adopt the assumption of the episodic lid regime, wherein Venus currently possesses a single, mature lithospheric lid and is inbetween resurfacing events.

A.3 Atla Regio

Atla Regio is a volcanic region located between 8°S and 9°N latitude and between 170°W and 150°E longitude. Its topography varies significantly, from approximately 700 m in Ningyo Fluctum at southeastern part of Atla Regio to 8800 m at the summit of Maat Mons. Other notable volcanoes in Atla Regio include Ozza Mons, Ongwuti Mons, and Uvaysi Mons. Geoid height values in Atla Regio range from 70 m to 150 m, while crustal thickness estimates vary between 8 km and 33 km (James et al., 2013). The region is primarily composed of radial

rift zones, lobate plains, and shield clusters, particularly in the highest elevations around Ozza Mons and Maat Mons.

Lava flow emissivity studies, which correlate with surface weathering rates, suggest that Maat Mons' volcanic activity occurred between 9 My and 60 My (Brossier et al., 2021). Additionally, emissivity analyses indicate that the lavas from Maat Mons, Ozza Mons, and Ongwuti Mons originate from a different source than those of Sapas Mons, which is located northwest of Atla Regio.

Structural analysis of Atla Regio's rift zones and graben systems (El Bilali et al., 2023) suggests that the region's volcanic activity is driven by a single mantle plume centered beneath Ozza Mons. This plume is currently in the plume-head phase, with an estimated maximum age of 50 My. Overlapping lava flows further suggest that Ozza Mons is younger than Maat Mons.

B Tested 2D models

Below we present an overview of 2D models that we tested.

Parameter	Value
reference density ρ_0	$3300\,\mathrm{kg\,m^{-3}}$
thermal capacity c_p	$1200\,\mathrm{J\,K^{-1}\,kg^{-1}}$
thermal conductivity k	$3.96\,\mathrm{W\,m^{-1}\,K^{-1}}$
thermal expansivity α	$3 \cdot 10^{-5}\,\mathrm{K^{-1}}$
reference viscosity η_0	$10^{20}\,\mathrm{Pa\,s}$
diffusion creep prefactor A^{diff}	$9.1963 \cdot 10^{-9}$
activation energy E_a^{diff}	$2.4 \cdot 10^{5}\,\mathrm{J\,mol^{-1}}$
Drucker-Prager cohesion C	$10\,\mathrm{MPa}$
Drucker-Prager friction μ	0.013
partition coefficient of water K	$2.1 \cdot 10^{-2}$
minimum viscosity η_{min}	$10^{20}\,\mathrm{Pa\,s}$
maximum viscosity η_{max}	$10^{24}\,\mathrm{Pa\,s}$
heat source density h	$6.5 \cdot 10^{12}\,\mathrm{W\,kg^{-1}}$
gravity g	$8.87\,\mathrm{m\,s^{-2}}$
extents	$730\,\mathrm{km} \times 7300\,\mathrm{km}$
basal resolution	1×10
minimum refinement	2
initial global refinement	2
initial adaptive refinement	3

Table B.1 Material parameters for initial model IM-A.

Model	Cohesion value
IM-A-C–0-5	$C = 0.5$ MPa
IM-A-C–1-0	$C = 1.0$ MPa
IM-A-C–5-0	$C = 5.0$ MPa
IM-A-C–7-5	$C = 7.5$ MPa
IM-A-C–10-0	$C = 10.0$ MPa
IM-A-C–15-0	$C = 15.0$ MPa
IM-A-C–20-0	$C = 20.0$ MPa
IM-A-C–30-0	$C = 30.0$ MPa
IM-A-C–50-0	$C = 50.0$ MPa
IM-A-C–100-0	$C = 100.0$ MPa

Table B.2 Changes in material parameters for initial models IM. Unspecified parameters are left the same as in model IM-A.
In these models we observe three main tectonic regimes, which we discuss in figure 2.1.

Model	Thermal anomaly amplitude
RM-T–25	$T_{\text{anom}} = 25$ K
RM-T–35	$T_{\text{anom}} = 35$ K
RM-T–50	$T_{\text{anom}} = 50$ K
RM-T–75	$T_{\text{anom}} = 75$ K
RM-T–100	$T_{\text{anom}} = 100$ K
RM-T–125	$T_{\text{anom}} = 125$ K
RM-T–150	$T_{\text{anom}} = 150$ K

Table B.3 Changes in material parameters for 2D regio models RM. Unspecified parameters are left the same as in model IM-A-C–50-0. At the bottom boundary a sixth order Gaussian thermal anomaly is prescribed at $x = 3000$ km, with width $\sigma = 35$ km and activity time $t_A = 100$ My. The amplitude of the prescribed thermal anomaly is varied.
These models show that significant melting appears only if the temperature contrast is higher than 50 K. The total topography increases with increasing temperature.

Model	Value of the varied parameter
RM-S–25	$\sigma = 25$ km
RM-S–30	$\sigma = 30$ km
RM-S–35	$\sigma = 35$ km
RM-S–40	$\sigma = 40$ km
RM-S–50	$\sigma = 50$ km
RM-S–60	$\sigma = 60$ km
RM-S–70	$\sigma = 70$ km
RM-S–80	$\sigma = 80$ km
RM-TA–50	$t_A = 50$ My
RM-TA–75	$t_A = 75$ My
RM-TA–125	$t_A = 125$ My
RM-TA–150	$t_A = 150$ My
RM-TA–175	$t_A = 175$ My

Table B.4 Changes in material parameters for 2D regio models RM. Unspecified parameters are left the same as in model RM-T–75. The width of the prescribed thermal anomaly and its activity time are varied.
Results of RM-S models lead to a conclusion, that σ of the temperature anomaly required for melt to occur is greater than 35 km. If we ignore the unrealistic central peak appearing due to the rifting effects, the best-fit model is recieved for $\sigma = 60$ km. Higher σ leads to overall higher peak.
Results of RM-TA models indicate, that t_A required for melting to occur is greater than 100 My. Later, the increasing t_A does not result in increasing the topographic peak, on the contrary, it seems to decrease the total topography. We believe this effect is purely numerical, as longer activity of the plume may cause significant lateral displacement of the depleted material and therefore unrealistic smoothing of the crustal topography.

Model	Value of the varied parameter
RM-DCP–60	$A^{\text{diff}} = 10^{-6}$
RM-DCP–65	$A^{\text{diff}} = 3.16 \cdot 10^{-7}$
RM-DCP–70	$A^{\text{diff}} = 10^{-7}$
RM-DCP–75	$A^{\text{diff}} = 3.16 \cdot 10^{-8}$
RM-PF–06	$A^{\text{diff}} = 0.6 \cdot 10^{-8}$
RM-PF–08	$A^{\text{diff}} = 0.8 \cdot 10^{-8}$
RM-DCP–80	$A^{\text{diff}} = 10^{-8}$
RM-PF–14	$A^{\text{diff}} = 1.4 \cdot 10^{-8}$
RM-PF–18	$A^{\text{diff}} = 1.8 \cdot 10^{-8}$
RM-PF–22	$A^{\text{diff}} = 2.2 \cdot 10^{-8}$
RM-PF–26	$A^{\text{diff}} = 2.6 \cdot 10^{-8}$
RM-DCP–85	$A^{\text{diff}} = 3.16 \cdot 10^{-9}$
RM-DCP–90	$A^{\text{diff}} = 10^{-9}$
RM-MV–01	$\eta_{\text{min}} = 0.1 \cdot 10^{20}$ Pa s
RM-MV–02	$\eta_{\text{min}} = 0.2 \cdot 10^{20}$ Pa s
RM-MV–04	$\eta_{\text{min}} = 0.4 \cdot 10^{20}$ Pa s
RM-MV–06	$\eta_{\text{min}} = 0.6 \cdot 10^{20}$ Pa s
RM-MV–08	$\eta_{\text{min}} = 0.8 \cdot 10^{20}$ Pa s
RM-MV–12	$\eta_{\text{min}} = 1.2 \cdot 10^{20}$ Pa s

Table B.5 Changes in material parameters for 2D regio models RM with a fixed plume. Unspecified parameters are left the same as in model RM-S–60.
Models RM-DCP and RM-PF demonstrate that increasing the stiffness (and thickness) of the lithosphere increases the width of the generated topography (however not the width of the unrealistic topographic peak). This observation is important as no other parameter was observed to have the same effect of significant magnitude. For our plume, the melting disappears for prefactor greater than $1.8 \cdot 10^{-8}$
Models RM-MV reveal that our plume is able to generate melt only if the minimum viscosity (upper mantle viscosity) is greater than $0.8 \cdot 10^{20}$ Pa s. Lower viscosity leads to plume not being able to thin the lithosphere enough and the hot material does not reach lower pressures (instead the plume starts to spread beneath the lithosphere).

C Chosen preliminary 3D models

In this attachment, we describe some of our preliminary 3D models. In these models, we assume isostatic compensation (no elastic flexure of the lithosphere) and we do not calculate the geoid yet. The models' topography is shifted in the vertical direction to properly overlap with the observed topography. Below the topographic comparison, we show a snapshot of the temperature beneath the uplifted Regio, where thick contours are isotherms of non-adiabatic temperature (as the plume is best observed in non-adiabatic temperature).

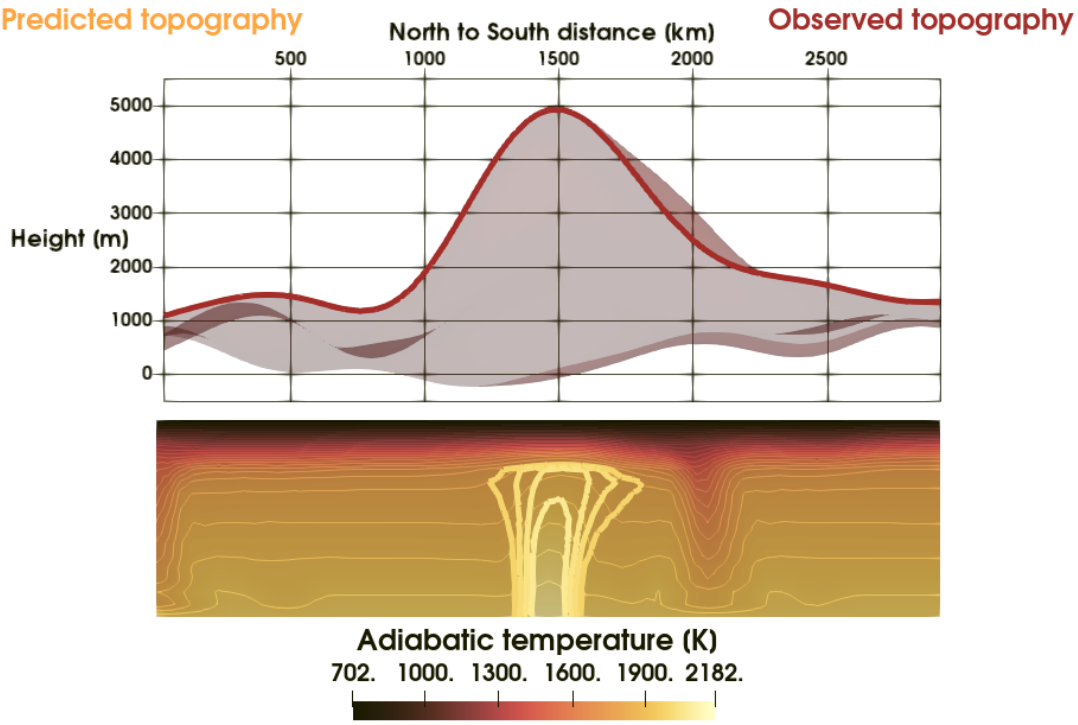
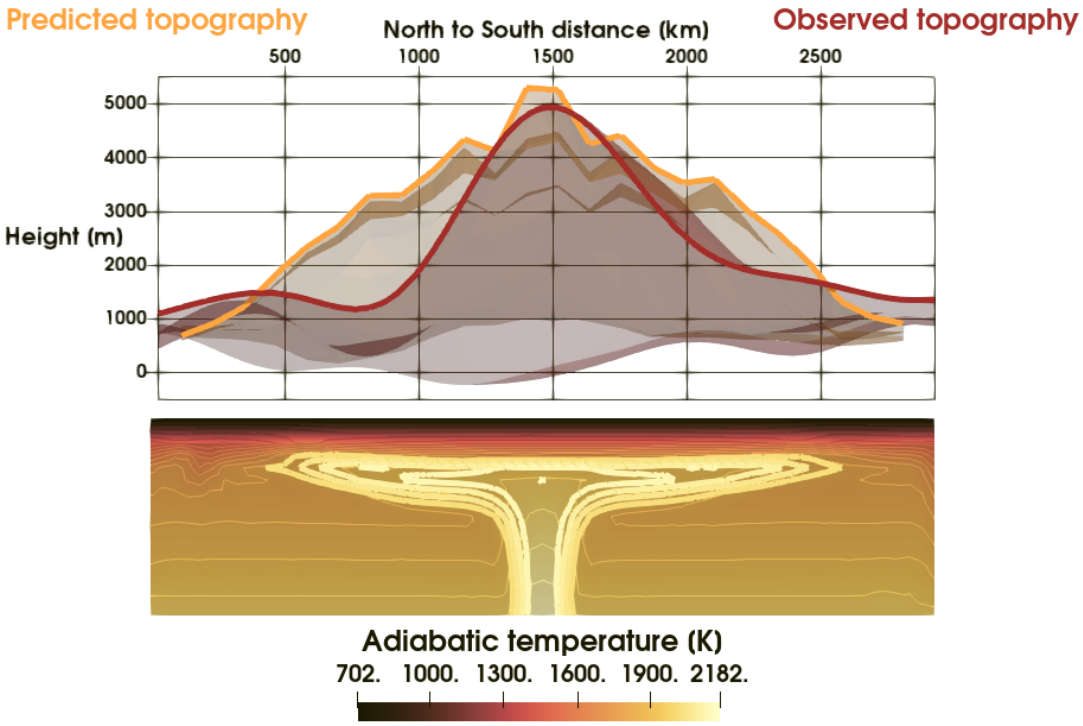


Figure C.1 Topography and convection of the preliminary model A (RM3D-HV). No melting is observed and therefore no topography is plotted (as only dynamic component of the topography is non-zero).

(a) around 80 My of model evolution



(b) around 200 My of model evolution

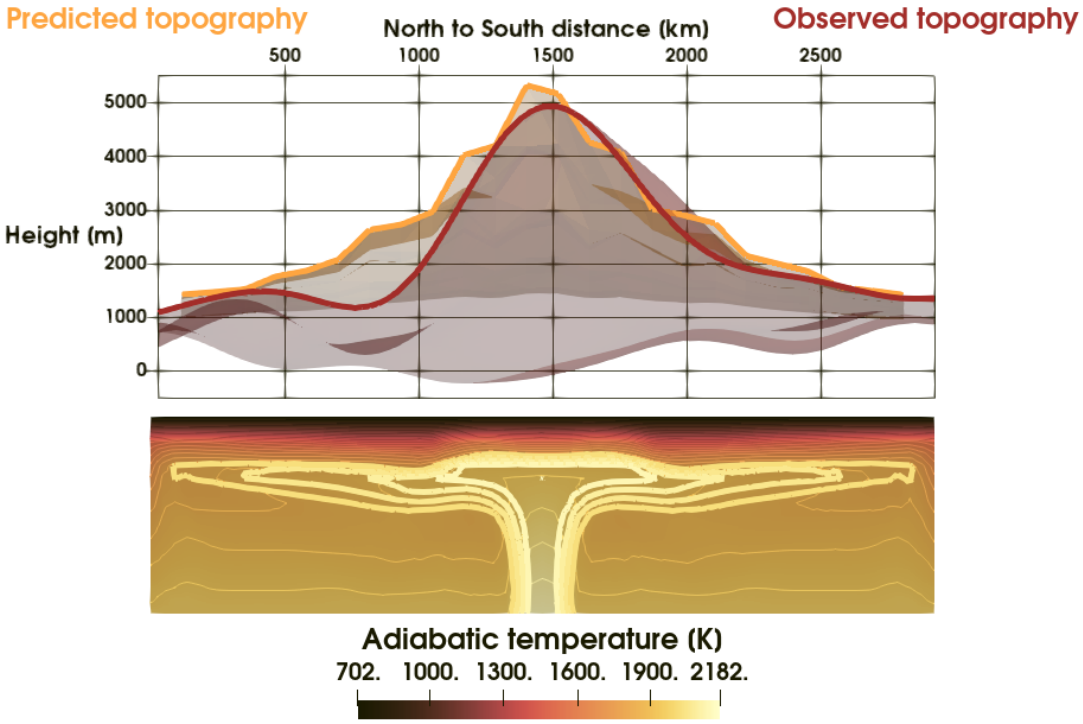


Figure C.2 Topography and convection of the preliminary model B (RM3D-HT). We observe an intesive spreading of the plume leading to both wide crustal topography and wide dynamic topography. (b) In the later stage of the evolution the plume spreads even further while maintaining similar topography. Numerical effects might cause lateral smoothing of the crustal topography.

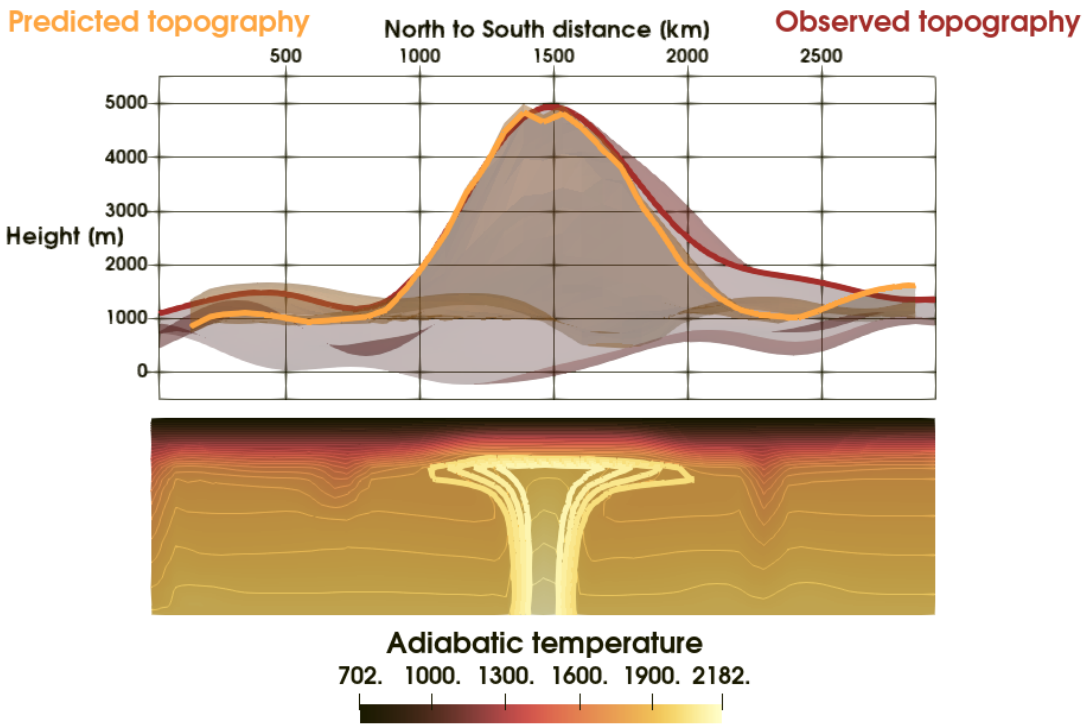


Figure C.3 Topography and convection of the preliminary model C (RM3D-HVHT). As we can see, this model is already fairly close to the observed topography and therefore we used this model as a basis for our best-fit model C2 (through model 20-ATLA-A).

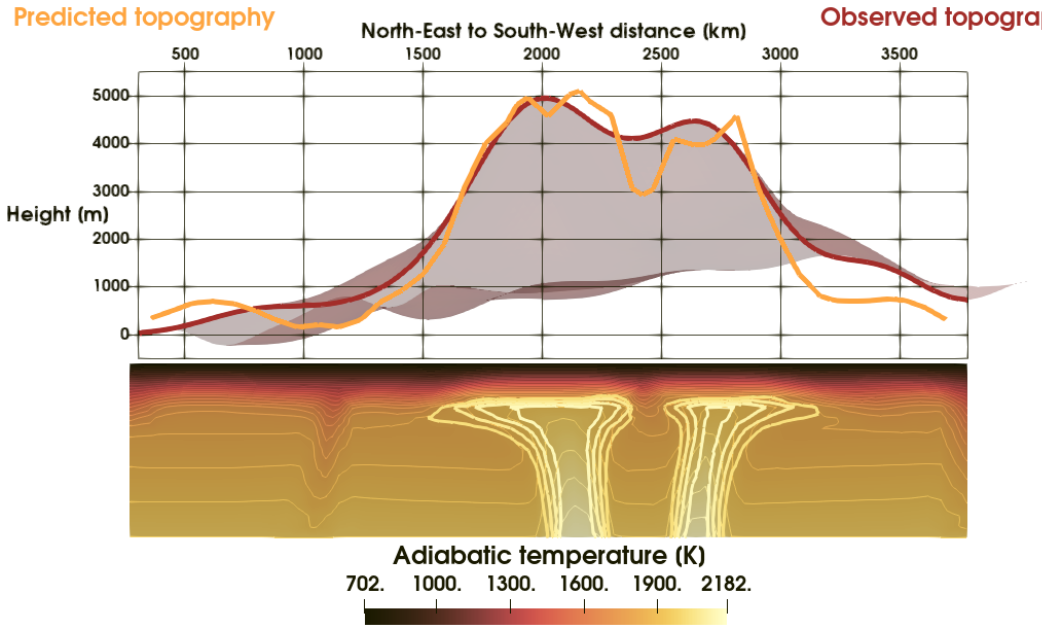


Figure C.4 Topography and convection of the preliminary model CCH-2. As we can see, prescribing a more complex plume in the upper mantle leads to a more complex double-peak topography. We assume the geoid would also be of a double-peak nature.

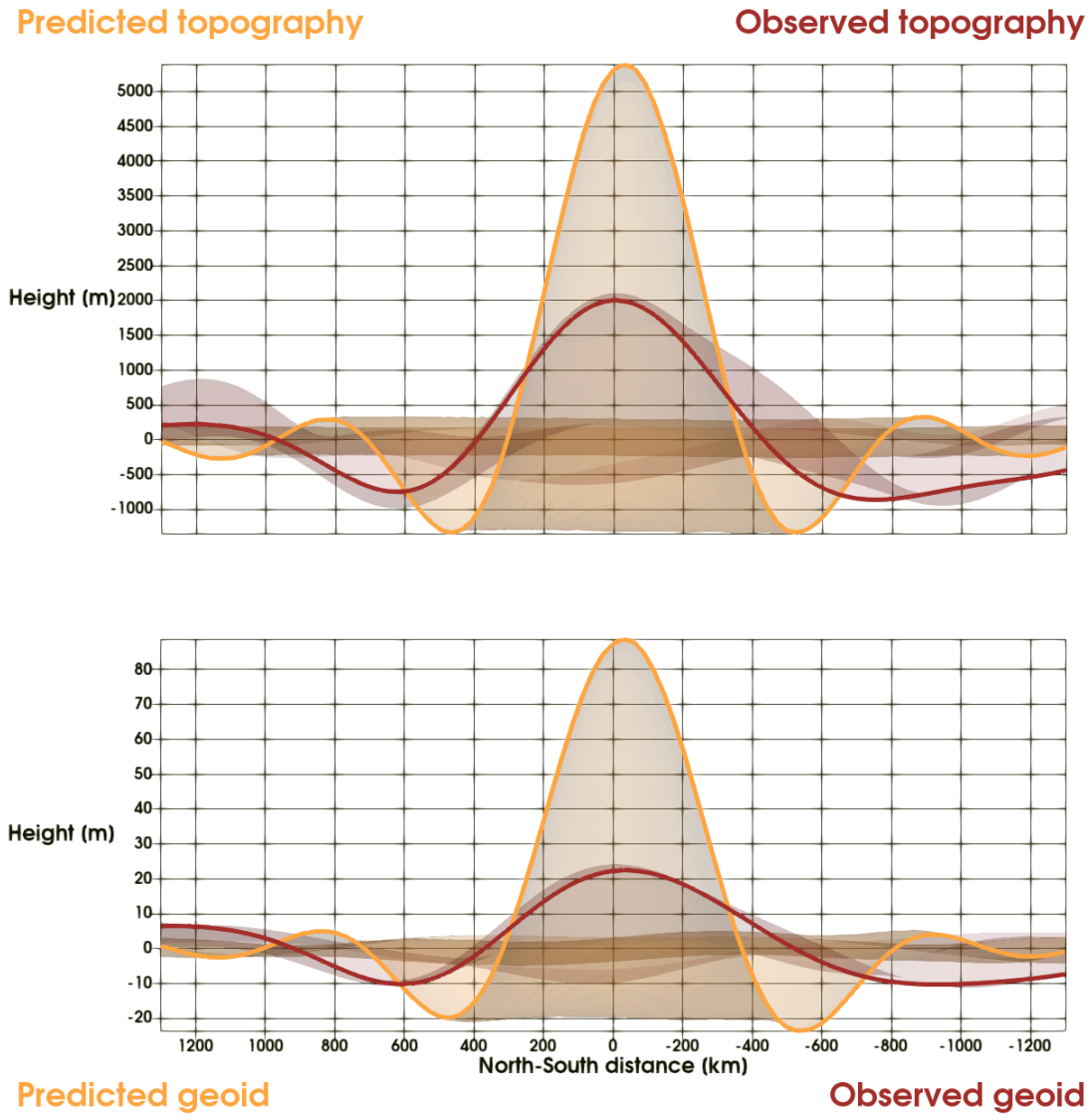


Figure C.5 Topography and geoid of model C2e2 with elastic thickness of 100 km. The model is reaching topography of 5000 m and generates a very high geoid, but the geoid is very localized, which is not the case for Atla Regio (see figure 1b or 2b).